Verification & Validation of CFD predictions regarding Pressurized Thermal Shock (PTS) situations in ROCOM installation: Comparison with IAEA Benchmark

Ayad, F.; Baghdad, M.; Bouaichaoui, Y.; Höhne, T.;

Originally published:

July 2023

Nuclear Engineering and Design 413(2023), 112498

DOI: https://doi.org/10.1016/j.nucengdes.2023.112498

Perma-Link to Publication Repository of HZDR:

https://www.hzdr.de/publications/Publ-37232

Verification & Validation of CFD predictions regarding Pressurized Thermal Shock (PTS) situations in ROCOM installation: Comparison with IAEA Benchmark

Fouad Ayad [a,] *, Mohammed Baghdad [a], Youcef Bouaichaoui [b], Thomas Höhne [c]

[a] Faculty of Science and Technology, Tissemsilt University, B.P. 182, 38000 Tissemsilt, Algeria

[b] Birine Nuclear Research Center/CRNB/COMENA/ALGERIA, BO 180 – Aïn Oussera, 17 001 Djelfa, Algeria

[c] Helmholtz-Zentrum Dresden-Rossendorf (HZDR), Institute of Fluid Dynamics, Bautzner Landstraße 400 | D-01328 Dresden, Germany

*Corresponding author. E-mail address: fouad.ayad@univ-tissemsilt.dz

Abstract

The current paper documents the Computational Fluid Dynamics (CFD) code validation activity, carried out at the Nuclear Research Center of Birine relevant of Atomic Energy Commission of Algeria as part of International Atomic Energy Agency (IAEA) Coordinated Research Project (CRP): Application of Computational Fluid Dynamics Codes for Nuclear Power Plant Design to assess the current capabilities of these codes and to contribute to technological progress in their verification and validation. A set of ROCOM CFD-grade test data of Pressurized Thermal Shock test (PTS) specifications was made available in the framework of this (CRP) by Helmholtz Zentrum Dresden-Rossendorf, (HZDR) Germany, to perform detailed calculations of the proposed test. The reference point is the injection of relatively cold core cooling water (ECC), which can induce buoyant stratification. The data obtained from the PTS experiment were compared with the results of Ansys-CFX calculations in this paper. Unsteady Reynolds-Averaged Navier-Stokes (URANS) model is used to examine the buoyancy-influenced flows in the reactor pressure vessel for condition where natural circulation is a dominant factor. The Shear Stress Transport (SST k-ω) turbulence model is used to take into account the turbulence effects on the mean flow. Calculation results show a good qualitative and quantitative agreement with the experiment data.

Keywords: *Verification & Validation, ROCOM, mixing,* ECC, *Ansys-CFX, IAEA, PTS, CRP*

1. Introduction

Over the past few decades, the scientific and power generation communities have been moving toward nuclear power plants operating at much higher capacity factors because, in the long run, we maintain that atomic fission technology is the only developed energy source capable of providing the enormous amount of energy that will be needed to run modern industrial societies, and doing so more energy security than other energy sources as renewable or fossil fuels that will be hard-pressed to supply the needed quantities of energy sustainably, economically and reliably. At the same time, the amount of gases radiation emitted by nuclear power is much lower than that emitted into the environment by other energy sources like fossil fuel. Accordingly, nuclear power produces heat without harmful gas and emits no pollution in the form of carbon dioxide. Although constructing a new nuclear power plant is expensive, operating costs are generally low because uranium is abundant and cheap.

Even though favorable data have been given for nuclear power plants, their safety and security characteristics are too complex. An uncontrolled or poorly moderated nuclear reaction in a nuclear reactor could lead to catastrophic acts such as fatigue wall or wall brittleness. Consequently, in this work we investigate the phenomenon of pressurized thermal shock (PTS) that occurs in nuclear reactors, which refers to a condition that threatens the integrity of the reactor pressure vessel (RPV).

The phenomenon of coolant mixing at different temperatures in the primary circuit of pressurized water reactors (PWR) plays an important role during normal operation and under accident conditions. Low-boron coolant slug can form in the cold branches of the primary circuit due to different mechanisms, e.g., in case of an untimely start of the first main coolant pump or the natural circulation that starts, the low-boron slug will be transported to the reactor core (IAEA-TECDOC-1908, 2020). In this case, the slug mixing phenomenon is the only mechanism responsible for mitigating a reactivity insertion due to a temperature perturbation created in one of the loops during an overcooling transient. The mixing of water slug of different temperatures is also very important for Pressurized Thermal Shock situations. In Emergency Core Cooling (ECC) situations after a Primary Loss of Coolant Accident (LOCA), ECC cold water is injected into the hot water of the cold branch and annular downcomer. Due to the large temperature differences, thermal shocks are induced at the reactor pressure vessel wall.

Computational fluid dynamics (CFD) experts envision the future application of codes, once they are properly verified and validated, to be a substitute for some of the expensive experimental testing associated with Nuclear Power Plant (NPP) design, as the use of such codes is capable of providing inexpensive qualitative and quantitative

information in many key areas for which traditional design tools are limited: i.e. where three-dimensional motions play a significant role. The technology is already well-established in other important industrial design areas, such as aerospace, automobile, chemical and turbo-machinery industries.

In this study, the use of three-dimensional CFD codes to predict the transient flows of the coolant mixing phenomenon related to thermal stratification is necessary, as these phenomena cannot be predicted by traditional one-dimensional codes with the for the development red accuracy and spatiotemporal resolution. The nuclear industry now recognizes that CFD codes have reached the desired level of maturity for use in the design process of nuclear power plants. To this end, the International Atomic Energy Agency (IAEA) has initiated a Coordinated Research Project (CRP): Application of Computational Fluid Dynamics (CFD) Codes for Nuclear Power Plant Design to evaluate the current capabilities of the various CFD codes and to contribute to the technological advancement of their verification and validation based on well-established experimental data, both for separate-effects tests and for full-scale integral tests. CFD is already well established to address certain safety issues in nuclear power plants. For developing, verifying, and validating CFD codes in respect to NPP design necessitates further modelling work on the complex physical processes involved, and on the development of the efficient numerical schemes required to solve the basic equations in an efficient manner, including advanced turbulence modelling. In parallel, it remains an overriding priority to benchmark the performance of such codes against experimental databases, in separate-effect tests and full-size integral tests. The scaling issue remains paramount to the component, but CFD allows to investigate the phenomena before proceeding to costly experiments. Therefore, the IAEA through the CRP has made available reference benchmarks of the so-called CFD-grade experiments performed on the ROCOM facility (IAEA-TECDOC-1908, 2020). The ROCOM facility is a 1:5 scale model based on the 4-loop Konvoi reactor concept. There are 1000 measuring points using the Wire-Mesh Sensor (WMS) measurement technique, for which data collection is available up to a frequency of 10 kHz (Prasser et al., 2003). It should be noted that each experiment was repeated five times to ensure reproducibility of the data. A CAD file of the test geometry is also provided. All test data is available in a detailed report for convenient interpretation (Höhne et al., 2018).

The benchmark experiments analyzed in this paper are provided by the Forschungszentrum Rossendorf, Dresden, HZDR, Germany, as part of the CRP by IAEA (IAEA-TECDOC-1908, 2020).These data of references are devoted to PTS scenarios. Density differences between the emergency cooling water and the primary loop inventory can play an important role during loss-of-coolant accidents in nuclear power plants, as the injection of the relatively cold ECC

water can induce buoyancy stratification. This stratification can causes high temperature gradients and increased thermal stresses of the reactor pressure vessel. In addition, in the case of accidental injection of low boron concentration ECC water, a boron dilution transient could be initiated, leading to unstable core operation. Such issues are of concern for the safety of the NPP, but they also need to be addressed at the design stage, as they directly influence on the expected lifetime of the plant.

The key issue related to the distribution of coolant properties is to know that if a coolant injection into the core after a Small Break Loss of Coolant Accident (SB-LOCA) can lead to pressurized thermal shock due to the relatively cold injected water not being sufficiently mixed with the water already present in the cold branches (Rohde et al., 2002).

From the data set, the d10m10 experiment with a 10% (constant) flow rate in a loop and a 10% density difference between the ECC and the loop water was selected for the calculations to be performed during this benchmark exercise (IAEA-TECDOC-1908, 2020). The Froude number for this test is Fr = 0.85, and thus it can be considered a dominated density. Since the ROCOM facility cannot be heated, the higher density of the cold ECC water is simulated by adding sugar (glucose). Buoyancy-related stratification is potentially dangerous and can result in strong temperature gradients and, consequently, high thermal stresses at the RPV (IAEA-TECDOC-1908, 2020). The validation is supported by the application of best practice procedures, BPG (NEA, 2015; NEA, 2007).

Although many studies of CFD modeling issues relevant to PTS have been investigated by experimental tests and numerical simulations in the international framework project initiated by several nuclear laboratories worldwide (OECD-NEA and in the CRP benchmark for NPP design organized by IAEA (IAEA-TECDOC-1908, 2020). The IAEA technical document comprehensively summarizes the ROCOM benchmark experiments related to PTS and the performance of the CFD experts. All the major CFD codes, i.e., Ansys-CFX, STAR-CCM +, Open-FOAM, etc., have participated, and a various turbulence models have been used, including Large Eddy Simulation (LES). Generally, the CFD results could predict the non-chaotic fluid behavior within an acceptable error range. However, the numerical predictions are less reliable for the flows in which the instabilities are prominent. Various turbulent models do not show significant differences between each other in the accuracy of the numerical results compared to the experimental data (IAEA-TECDOC-1908, 2020).

Moreover, several researchers have carried out a series of simulations using three-dimensional (3D) thermal-hydraulic codes on the ROCOM tests associated with the asymmetric natural circulation flow mixing transients. The outcomes of the assessment studies show qualitative agreements with the experimental data and the dynamic evolution of the

thermal stratification in the downcomer occurring during the transients are well reproduced. Compared to the results of CFD codes, 3D system codes provide similar prediction results regardless of the differences in physical modeling approaches and computational costs (Bieder et al., 2016; Bousbia Salah et al., 2018; Čarija et al., 2020; Chouhan et al., 2021; Farkas et al., 2016; Grunwald et al., n.d.; Höhne et al., 2018, 2011a, 2011b, 2008, 2004; Höhne and Kliem, 2022; Kliem et al., 2008; Loginov et al., 2011, 2010; Pandazis et al., 2015.; Puragliesi, 2020; Rohde et al., 2005.; Wei et al., 2022).

The remaining sections of this paper are organized as follows. Section 2 describes the ROCOM facilities and experiments in detail. Section 3 presents a characterization of the density impacts of ECC water injection. Section 4 deals with the mathematical modelling and simulation method. Finally, we can see the results of a comparison between numerical simulations and the PTS benchmark experiments. In this part, we present some works which have studied the scenario of thermal shock under pressure in the ROCOM facility. This phenomenon manifests at the level of the wall of the reactor vessel and threatens the safety of NPPs. Many studies have been done to compare CFD analyses and experimental measurements. The mixing scalar and the impact of flow density variations have both been modelled using different regimes (dXmY) with and without buoyancy, so according to the experimental data and numerical calculation, the influence of buoyancy between ECC water and inventory water was illustrated by the different form of propagations of the slug for each regime, in the first cold branch N°1 of injection, downcomer, core inlet. Thus, the mixing phenomenon and flow model are well predicted by Ansys-CFX and Trio-UCFD codes (Höhne et al., 2006).

On the other hand, after the development of computer hardware, and especially CFD codes, to distinguish the role of the mesh density and its sensitivity, the latest version of Trio-U CFD was used to recalculate a work done by (Höhne et al., 2006), with an old mesh. In this case, the number of mesh nodes is increased from 2M nodes (coarse) to 6.5M nodes(refined) for Ansys-CFX and it's increased from 3M nodes to 22M elements for Trio-CFD (Höhne et al., 2018). , the results show that the flow physics can be better represented today due to higher CPU power (Bieder et al., 2016). For the same reason, to study the influence of the computational grid density on stratification and buoyancy-driven, LES was involved in the single-phase PTS simulations. The results show that y^+ should be included in these intervals for meshes using LES for PTS case to obtain accuracy, so $y^+ = 40$ for momentum-driven flow in the cold leg, and $y^+ =$ 65 to 100 for buoyancy-driven flow in the RPV (Loginov et al., 2010).

In addition, after having done the mesh sensitivity in the previous section, we move on to the next section which contains the influence of the turbulence modeling.

three tests were used with different density differences and volume flow rates, to evaluate the influence of various turbulent heat flux models on the calculation of turbulent buoyancy production on the predictions of the turbulent mixing phenomenon occurring in ROCOM tests. The results are as follows URANS simulations with the turbulence models, i.e., (standard k-ε and SST k-ω), generally showed good agreement with the experimental data in terms of spatial average mixing scalar values measured in the downcomer and at the inlet core (Wei et al., 2022).

In the same context, three tests with different coolant regimes flow types were made, covering both low and high-density ratios, relatively low and high mass flows rate, and quasi-steady state and transient boundary conditions. Moreover, the k-ε turbulence model was used with different min and max Schmidt numbers. It has been found that decreasing the turbulent Schmidt number improves the predictions of spatially averaged quantities in all regions. Also, the study shows that URANS simulations are rather successful in describing quantitatively the mixing phenomenon (Puragliesi, 2020). The PTS phenomenon in the ROCOM facility was investigated with LES and RANS turbulence models. By comparing the CFD and measured results, it was noticed that the LES offers more prediction accuracy compared with the RANS model (Chouhan et al., 2021).

Most of the numerical studies on ROCOM tests mentioned in **Table 1** have mainly addressed on the influence of boundary conditions, geometrical representation, numerical mesh/nodalization and turbulence modeling, but very few have discussed the turbulent heat flux models which are essentially involved in the concentration/temperature transport equation.

The outcomes of a buoyancy driven mixing simulation conducted in the ROCOM facility are shown to be significantly influenced by the boundary conditions, initial conditions, and overall simulation settings that are used. Each of these elements plays a crucial role in the excellence and accuracy of the final solution (Čarija et al., 2020). Likewise, an evaluation of the mixing phenomenon in a ROCOM test was performed to provide results for comparison between experimental results and numerical calculations performed by thermo- hydraulic system codes with 3D capabilities (CATHARE, TRACE, ATHLET) and CFD codes (Ansys-CFX,Star CCM+). The results were rather similar, regardless of the difference in the physical approach between them (Bousbia Salah et al., 2018). Another element that must be mentioned in this part is the modeling of the multi-component flow. In this case, there is only a single-phase multi-component flow because the mixture shares the same mean velocity, pressure and temperature fields, and the mass transfer takes place by convection and diffusion (Ansys-CFX -Solver Modeling Guide, 2020).

Table 1. An overview of research on ROCOM implementation for PTS events.

Years	Authors	CFD codes	Mesh Number elements	Turb. models	Coupling methods	Density difference	Flow types	Discr. schemes
2004	(Höhne et al., 2004)	Trio-U	$3\times10^5 \div 2\times10^6$ elements	LES	explicit	d10m05	Density driven dominated	Second-order
2006	(Höhne et al., 2006)	CFX.5 Trio-U	4×10^6 elements 3×10^6 nodes	RSM (BSL) LES	implicit scheme	d10m05	Density driven dominated	Second-order
						d00m15	Momentum driven dominated	
2008	(Höhne et al., 2008)	Ansys-CFX	4×10^6 elements	RSM (BSL)	implicit scheme	d00m15 d02m15	Momentum driven dominated	Second-order
						d10m15 d05m10	Transition	
						d05m05 d10m10	Density driven dominated	
2010	(Loginov et al., 2010)		$3.01\times10^6 \div 12.26\times10^6$ elements	LES	implicit	d05m00	Density driven dominated	Second-order
2011	(Loginov et al., 2011)		$13.2\times10^6 \div 19.9\times10^6$ elements	LES	implicit	d05m05	Density driven dominated	Second-order
						d05m10	Transition	
						d05m15	Momentum driven dominated	
2011	(Höhne et al., 2011a)	CFX	6.5×10^6 elements	RSM (BSL)	implicit	d0-02m0	Density driven dominated	Second-order
2016	(Bieder et al., 2016)	Trio-U CFD	7.5×10^6 elements	LES	explicit	d10m05	Density driven dominated	Second-order
2018	(Höhne et al., 2018)	CFX	4×10^6 elements	RSM	explicit	d10m10	Density driven dominated	Second-order
		Trio-U	22×10^6 elements	LES		d00m15	Momentum driven dominated	
2018	(Bousbia et al., 2018)	CFX, Stare CCM+	$5\times10^6 \div 6.2\times10^6$ elements	SST k-ω k-ε	implicit semi-implicit	d038m(t)	Momentum	Second-order
2020	(Puragliesi, 2020)	Star CCM+	12×10^6 elements	k-ε	semi-implicit	d12m12 d1.28m10 d12m(t)	Transition Momentum Density driven	Second-order
2020	(Čarija et al., 2020)	Ansys fluent	8.5×10^6 elements	k-ε, k-ω, SST k-ω, RSM	segregated solver	d10m10	Density driven dominated	Second-order
2021	(Chouhan et al., 2021)	Open foam	$2.8\times10^6 \div 12\times10^6$ elements	SST k-ω, k-ε, LES	explicit	d10m10	Density driven dominated	Second-order
2022	(Wei et al., 2022)	Open foam	8.3×10^6 elements	k-ε SST k-ω	upwind	d12m12.2 d012m10.25 d12m(t)	Transition Momentum Density driven	Second-order
2022	(Höhne and Kliem, 2022)	Ansys-CFX	6.5×10^6	RSM (BSL)	Backward Euler	d00m15 d10m10	Density driven dominated	Second-order

The IAEA has long recognized that there will be increasing interest in the use of CFD codes, particularly in verification & validation and uncertainty quantification, and will join the OECD/NEA in sponsoring the first exploratory effort to document the progress of CFD as a simulation tool in the field of nuclear reactor safety, and advance it through

benchmarking exercises and international workshops. These joint activities are still ongoing. This CRP is intended to fill a gap in the original initiative in recognition of the increasing use of CFD tools in reactor design, while maintaining the existing synergy with ongoing efforts in the reactor safety area with the NEA (NEA, 2015; IAEA, 2022; Wang et al., 2021).

2. ROCOM facility and test description

The ROCOM test facility consists of a Perspex model of the RPV (**Fig.1**) with four inlet and four outlet nozzles (Prasser et al., 2003). The facility is equipped with four fully independent operating loops (**Fig.2**) each with its own circulation pump, driven by motors with computer-controlled frequency transformers. As a result of this setup, a wide variety of operating regimes can be realized: four-loop operation; operation with pumps off; simulated natural convection modes; and flow ranges. For the study of natural circulation modes, the pumps are operated at low speed using the frequency transformer system. Geometric similarity between the current Konvoi reactor and the ROCOM facility is maintained from the inlet nozzles to the downcomer and to the core inlet (the core itself is excluded from the similarity principle). All components of the ROCOM test facility are made from Perspex for visualization purposes (**Fig.1**).

An overview of the ROCOM test facility is given in **Fig.1**. The PWR model incorporates, at 1:5 scale, the original PWR geometry with respect to nozzle design (diameter, radii of the bending and diffusion sections), the characteristic extension of the downcomer cross-section below the nozzle area, the perforated drum in the lower plenum, and the design of the core support plate with its ports for the passage of coolant into the core. The flow rate through the loops is scaled to the transit time of the coolant through the RPV. That is, the coolant transit time in the model is identical to that in the reactor when the actual coolant flow rate is reduced by 1:5.

Fig.1. Perspex model of the RPV in ROCOM (IAEA-TECDOC-1908, 2020).

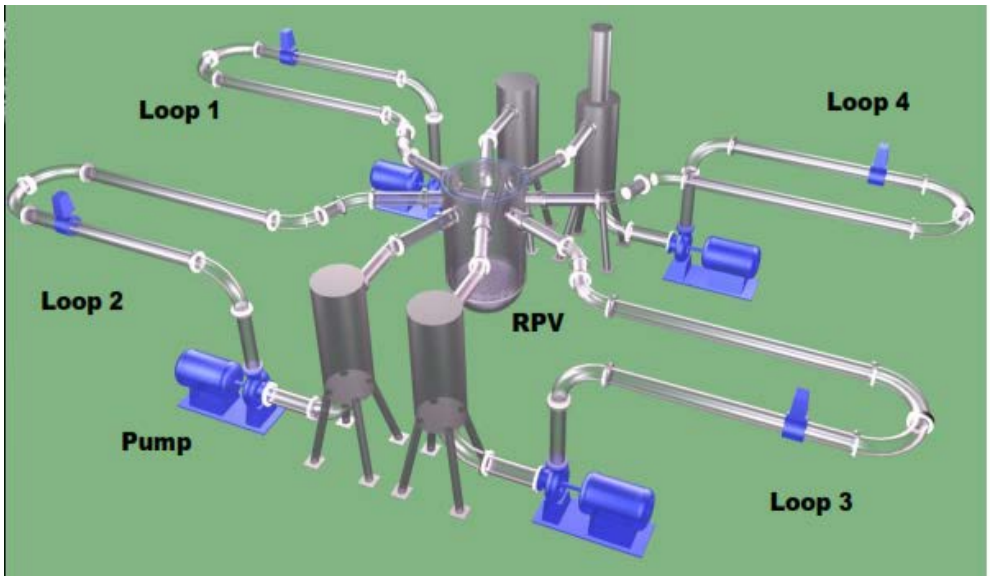

Fig.2. Overview of the ROCOM test facility with its four loops and individual frequency-controlled circulation pumps (Bieder et al., 2016).

From these scaling laws, the nominal volumetric flow rate in ROCOM is 185 m³/h per loop. The Reynolds numbers are about half as small as in the reactor. Due to the reduced geometry, a factor of 25 applies to the mass flows, and thus to the velocities (Höhne et al., 2006). The remaining differences arise from operation at room temperature at and atmospheric pressure. In particular, at room temperature, the viscosity of water is about 8 times higher than at typical reactor conditions. Since coolant mixing is primarily turbulent dispersion induced (i.e., largely independent of the exact molecular properties of the fluid), it is possible to use a tracer substance to model differences in boron concentration or coolant temperature. The coolant in the perturbed loop is tagged by injecting a sodium chloride (common salt) solution into the main coolant stream upstream of the reactor inlet nozzle. Magnetic valves are used to control the injection process (Pandazis et al., 2015).

Since the ROCOM facility cannot be heated, the higher density of the cold ECC water is simulated by adding sugar (glucose). In the d10m10 experiment described here, a density difference of 10% was used. A sugar solution with a density of 1100 kg/m³ has a viscosity that is a factor of 3 higher than pure water. The sugar tracer can therefore still be considered a low viscosity fluid (Höhne et al., 2006).

The distribution of the tracer in the water flow field was measured using electrode mesh sensors, which sample the distribution of electrical conductivity over the flow cross section. The development of these sensors aimed to produce a direct conductivity measurement between pairs of crossed wires to avoid the use of tomographic reconstruction

algorithms (Prasser et al., 1998, Prasser et al., 2001), and to achieve a temporal resolution of up to 10 000 frames per second (Prasser et al., 2002). In this technique, two electrode-crossing grids (insulated from each other) are placed transversely the cross-section of the flow duct. The electrodes of the first grid (emission electrodes) are successively charged with short voltage pulses. The currents arriving at the electrodes of the second grid (receiving electrodes) are recorded. After a complete cycle of transmitter activation, a full *2D* matrix of local conductivities is obtained. Special signal acquisition methods (Prasser et al., 2002) ensure that each value of the matrix depends only on the local conductivity in the immediate vicinity of the corresponding crossing point between the transmitter and receiver electrodes.

In the current test, the mesh sensors are placed at four positions in the flow path. The first sensor (**Fig.3**) is flanged to the reactor inlet nozzle in **Fig.** (**1,2**) in loop N°1 and records the tracer concentration at the reactor inlet. The second and third sensors are located at the inlet and outlet of the downcomer. The downstream sensors consist of 64 radial mounting rods with holes for four circular electrode wires (**Fig.4**) Small ceramic insulating balls electrically separate the rods and wires. The rods act as radial electrodes; each rod corresponds to a circumferential measurement position.

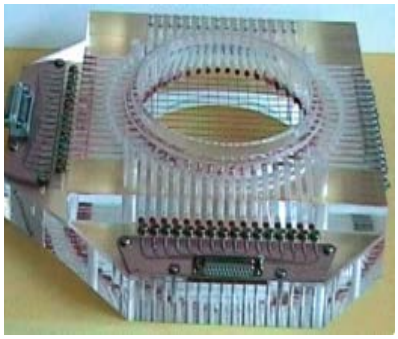

Fig.3. Mesh sensor for measuring tracer distributions in front of the reactor inlet nozzle (Höhne et al., 2006).

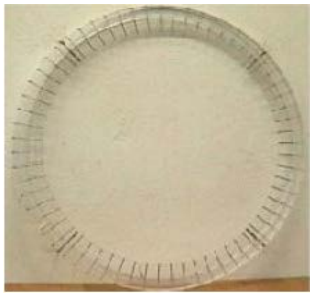

Fig.4. Wire mesh sensor in the downcomer for radial measurements (64x4 measuring positions) (Puragliesi, 2020; Höhne et al., 2006).

The fourth sensor is integrated into the core support plate (**Fig. 5**), 2×15 electrode wires are arranged so that the wires of the two planes intersect in the centers of the coolant inlet ports of each fuel element. In this way, the tracer concentration can be measured for each individual fuel element channel.

In total, signals from approximately 1000 measurement points are composed, each at a frequency of 200 Hz. In most cases, 10 successive measurements are taken, averaged, and the result stored (at a frequency of 20 Hz). The characteristic frequency of the phenomena observed in this ROCOM test does not justify a sampling frequency higher than this. The measured local conductivities are then related to standard reference values. The result is a mixing scalar that instantly characterizes the coolant from the perturbed loop (i.e., the one into which the tracer was injected) at any given location within the flow field. This scalar is dimensionless (Höhne et al., 2004).

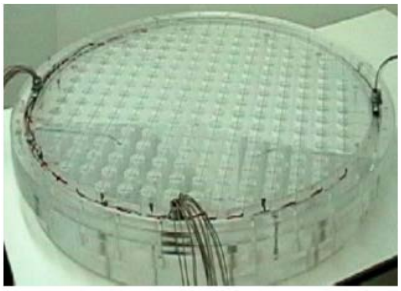

Fig.5. Wire-mesh sensor in the core inlet plane(Kliem et al., 2008; Höhne et al., 2006) .

3.Density impacts by ECC water injection

Different experiments can be performed by assuming similarity between the tracer concentration and the temperature and boron concentration fields, which gives the ROCOM center great flexibility. As standard, the reference values correspond to the unaffected coolant (index “0”) and the coolant at the “disturbed” reactor inlet nozzle (index “1”). The difference between the two reference values is the magnitude of the disturbance. A mixing scalar $\theta_{x,y,z,t}$ can therefore be defined as follows (Höhne et al., 2008):

$$\theta_{x,y,z,t} = \frac{\sigma_{x,y,z,t} - \sigma_0}{\sigma_1 - \sigma_0} \cong \frac{T_{x,y,z,t} - T_0}{T_1 - T_0} \cong \frac{C_{x,y,z,t} - C_{B,0}}{C_{B,1} - C_{B,0}} \tag{1}$$

Where $\sigma_{x,y,z,t}$ denotes the electrical conductivity (measured), T is the temperature (derived), and C_B is the boron concentration (derived). Each of the two parameters - temperature or boron concentration - is represented by the measured mixing scalar and depends on the appropriate choice of reference values and stipulation of the boundary conditions of the experiment (Höhne et al., 2008).

For low-viscosity coolant solutions, a simple linear relationship can be assumed to transform the conductivities recorded by the sensors into dimensionless scalar concentrations. However, this proved insufficient for the glucose-water mixtures used in some ROCOM tests, including d10m10, for which a nonlinear correlation applies. The presence of sugar shown in **Fig.6** alters the linear relationship between the electrical conductivity signal recorded by the wire mesh sensors and the actual mixing scalar defined by the concentration level of the sugar (Höhne et al., 2006). The correlations were verified using separate mixing tests in which conductivity was measured for specified values of the mixing scalar. the two solid black lines give the results for two values of conductivity, and are well correlated with the measured data.

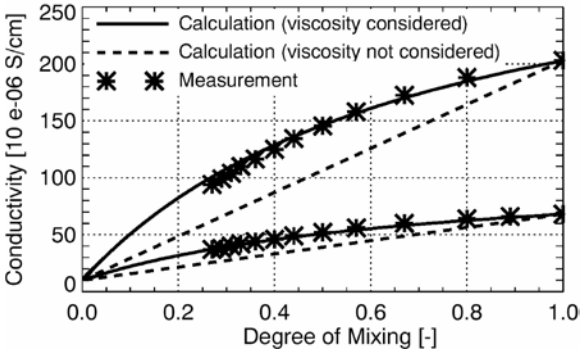

Fig.6. Effect of viscosity on the conductivity measured and the degree of mixing scalar for two conductivity values (Höhne et al., 2004).

The functional relationship depends on the normalized viscosity of the mixture, which is proportional to the density of the mixture. In particular, the dynamic viscosity is a non-linear function of the sugar concentration. The sugar solution with a corresponding density of 1100 kg/m^3 has a viscosity that is by a factor of 3 higher than that of pure water, as shown in **Fig.7**. The sugar tracer can, therefore, still be visualized as a fluid with low viscosity (Höhne et al., 2018).

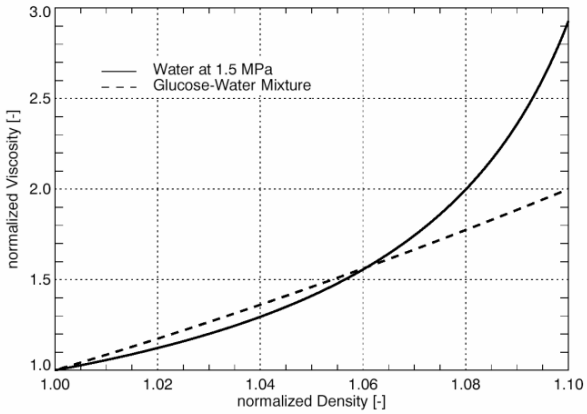

Fig.7. Evaluation of the normalized viscosity of water and of the glucose–water combination used in the ROCOM experiments (Höhne et al., 2018).

The objective of the series of PTS experiments conducted in ROCOM was to study the effects of density differences between the primary loop inventory and the water injected by the ECC during mixing in the downcomer. The mass flow rate was varied between 0 and 15% of the design flow rate; that is, it was kept at the same order of magnitude as that of the natural convection mode. The density difference between the ECC and loop water varied between 0 and 10% (IAEA-TECDOC-1908, 2020). The boundary conditions used in the experiments are all pictorially shown in **Fig.8**. such that a total of 21 experiments were achieved to form the test matrix presented the analysis of all experiments (IAEA-TECDOC-1908, 2020). In their paper, the authors develop a criterion for distinguishing between momentum-driven and density-driven flows based on the experimental data composed from these tests. By the densiometric Froude number, defined in the usual way:

$$Fr = \sqrt{\frac{\rho v^2}{\nabla \rho \cdot g \cdot l}} \tag{2}$$

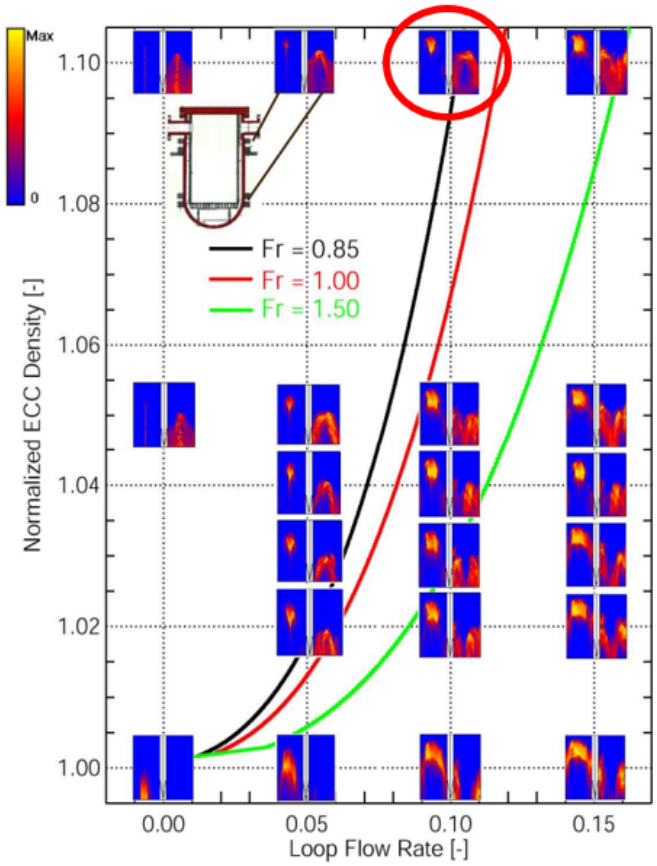

Fig.8. Assessment matrix of ECC injection experiments, picturing of the time dependent tracer distribution at the sensors in the downcomer (Höhne et al., 2018).

Where v is the velocity, ρ is the density of the fluid, g the gravitational acceleration, l the characteristic length of downcomer and $\Delta\rho$ is the density difference between the coolant inventory and the slug. From the data set, the experiment with 10% (constant) flow rate in a loop and 10% density difference between the ECC and the loop water was designated for calculations to be executed during this benchmark exercise (Höhne and Kliem, 2022).The Froude number for this test is Fr = 0.85, and thus can be considered a dominated density.

4. Mathematical modelling and simulation method

4.1 Physical domain

The analysis has been performed with Ansys-CFX -2022.R1 code for simulations of turbulent flow and mixing in ROCOM facility by solving the Unsteady Reynolds Averaged Navier Stokes (URANS) equations with k-ω SST turbulence model associate with a transport equation of an additional, user-defined, scalar variable simulating the tracer. The Shear Stress Transport (SST) model was designed to give highly accurate predictions of the onset and the amount of flow separation under adverse pressure gradients by the inclusion of transport effects into the formulation of the eddy viscosity. This results in a major improvement in terms of flow separation predictions. The superior performance of this model has been demonstrated in a large number of validation studies (Bestion, 2012). Based on the comparison the SST turbulence model was chosen for the further simulations, which unifies the advantages of two-equation (k-ω and k-ε) models. Furthermore, according to BPG, validation is the process of determining how precisely a model captures reality or experiment data. Verification is the process of ensuring that a program solves equations correctly (Kliem et al., 2010; NEA, 2015; NEA, 2007).

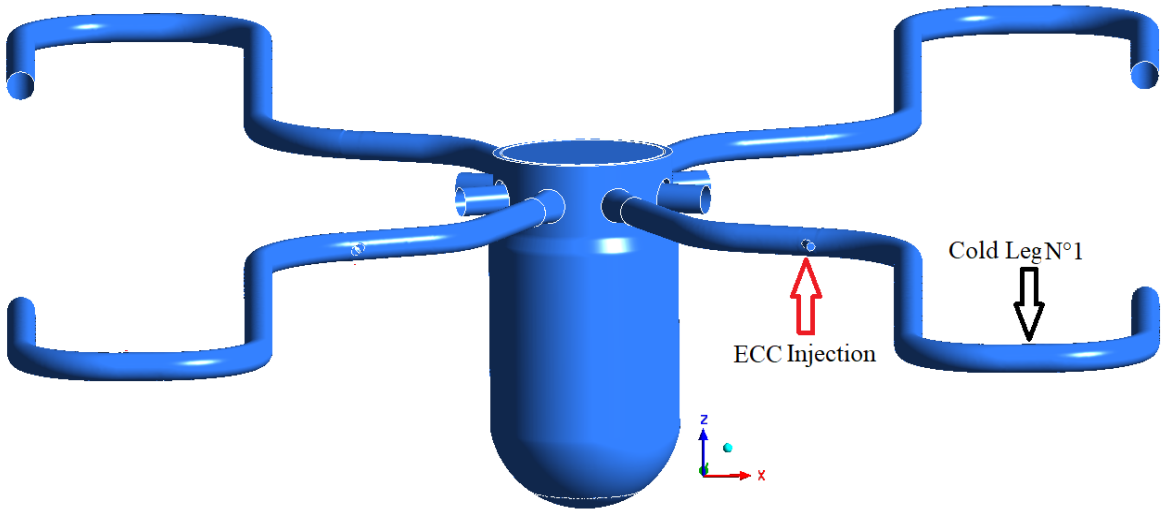

Fig.9. Physical domain of ROCOM mock up.

For the study presented here, the Boussinesq approximation is applied to take into account density effects on the momentum equation. The density is assumed constant in all terms of the Navier-Stokes equations except the gravity term. The buoyancy and dissipation terms were introduced into the turbulent kinetic energy equation. There, the density is a function of the local temperature.

The discretization in space is a 2nd order element-based finite-volume method with 2nd order time integration. It uses a coupled algebraic multigrid algorithm to solve the linear systems arising from discretization. The discretization schemes and the multigrid solver are scalable parallelized. CFX works with unstructured hybrid grids consisting of tetrahedral, hexahedral, prism and pyramid elements (NEA, 2015; NEA, 2007).

4.2 Governing equations

The water flow within the ROCOM installation is considered unsteady, incompressible and 3D. Equations composed the *CFD* model used are briefly described in this section. The *CFD* model solves the unsteady averaged Navier-Stoke equations:

$$\frac{\partial}{\partial x_i}\left(\rho u_i\right) = 0 \tag{3}$$

$$\frac{\partial\left(\rho\overline{u}_i\right)}{\partial t} + \frac{\partial}{\partial x_i}\left(\rho\overline{u}_i\,\overline{u}_j\right) = -\frac{\partial\overline{p}}{\partial x_i} + 2\mu\left(\frac{\partial\overline{S}_{ij}}{\partial x_j}\right) - \frac{\partial\tau_{ij}}{\partial x_j} + F_i \tag{4}$$

$$\frac{\partial\left(\rho\overline{m}_w\right)}{\partial t} + \frac{\partial}{\partial x_i}\left(\rho\overline{u}_i\,\overline{m}_w\right) = \frac{\partial}{\partial x_j}\left[\left(\rho D + \frac{\mu_t}{Sc_t}\right)\frac{\partial\overline{m}_w}{\partial x_i}\right] \tag{5}$$

Where $\overline{S}_{ij} = \frac{1}{2}\left(\frac{\partial\overline{u}_j}{\partial x_i} + \frac{\partial\overline{u}_i}{\partial x_j}\right)$; $\tau_{ij} = \rho\left(\overline{u_i u_j} - \overline{u}_i\overline{u}_j\right)$;ρ, u_i and p denote density, velocity components and static pressure.

μ_t is the turbulent viscosity and τ_{ij} is the Reynolds stresses. The term F_i stands for the Reynolds-averaged buoyancy force which couples the momentum equations and the energy equation in the case of mixed convection and following the Boussinesq approximation, it can be expressed as:

$$F_i = -\beta\left(\theta - \theta_0\right)g_i \tag{6}$$

where θ_0 is the reference temperature, β is the volumetric thermal expansion coefficient and g_i is the gravitational acceleration vector.

A turbulence model is needed to model the unknown Reynolds stresses through turbulent eddy viscosity, μ_t. In the present study, the *SST k-ω* turbulence model (Menter, 1994) is used.

The turbulence kinetic energy k, and the specific dissipation rate ω, are obtained from the following transport equations:

$$\frac{\partial}{\partial t}(\rho k)+\frac{\partial}{\partial x_i}(\rho k u_i)=\frac{\partial}{\partial x_j}\left(\left(\mu+\frac{\mu_t}{\sigma_k}\right)\frac{\partial k}{\partial x_j}\right)+G_k-Y_k+S_k \quad (7)$$

$$\frac{\partial}{\partial t}(\rho \omega)+\frac{\partial}{\partial x_i}(\rho \omega u_i)=\frac{\partial}{\partial x_j}\left(\left(\mu+\frac{\mu_t}{\sigma_\omega}\right)\frac{\partial \omega}{\partial x_j}\right)+G_\omega-Y_\omega+S_\omega \quad (8)$$

where μ_t is the turbulent viscosity and σ is the turbulent Prandtl number. G_k and G_ω represent production terms of the turbulent kinetic energy k and specific dissipation rate ω due to the Reynolds-averaging velocity gradient tensor; and Yk and Y_ω correspond to the dissipation terms of the turbulent kinetic energy and the specific dissipation rate. S_k and S_ω are user-defined source terms.

4.3 Grid generation

The numerical mesh was created by Ansys-ICEM CFD with unstructured hybrid grids consisting of tet, hex, prism and pyramid elements. The investigated mixing phenomena occur in the Cold Leg N°1 during the ECC injection, in the downcomer and lower plenum. All domain from the cold leg to the core support plate has been discretized with fine mesh resolution. The number of mesh cells of different mesh types is summarized in Table 2. A total view of the mesh is shown in **Fig.10**.

Table.2: Grid information

Mesh type	**Number of cells**
Hex	2 377 780
Tet	3 222 496
prisms	859 410
pyramids	29 131
Total number of cells	**6 488 817**

Approximately 1000 monitor points that were placed in four positions similar to the positions of the sensors measuring the electrical conductivity (**Fig. 11**). So, as a transient process is investigated, these points must be placed in CFX-Pre to acquire all variables that change as a function of time, especially the mixing scalar, which is a dimensionless number. The data of these points are taken from the file by Cartesian and cylindrical coordinates. The comparison of experimental and CFD data is done in four sensors (RPV inlet, upper and lower downcomer, core inlet).

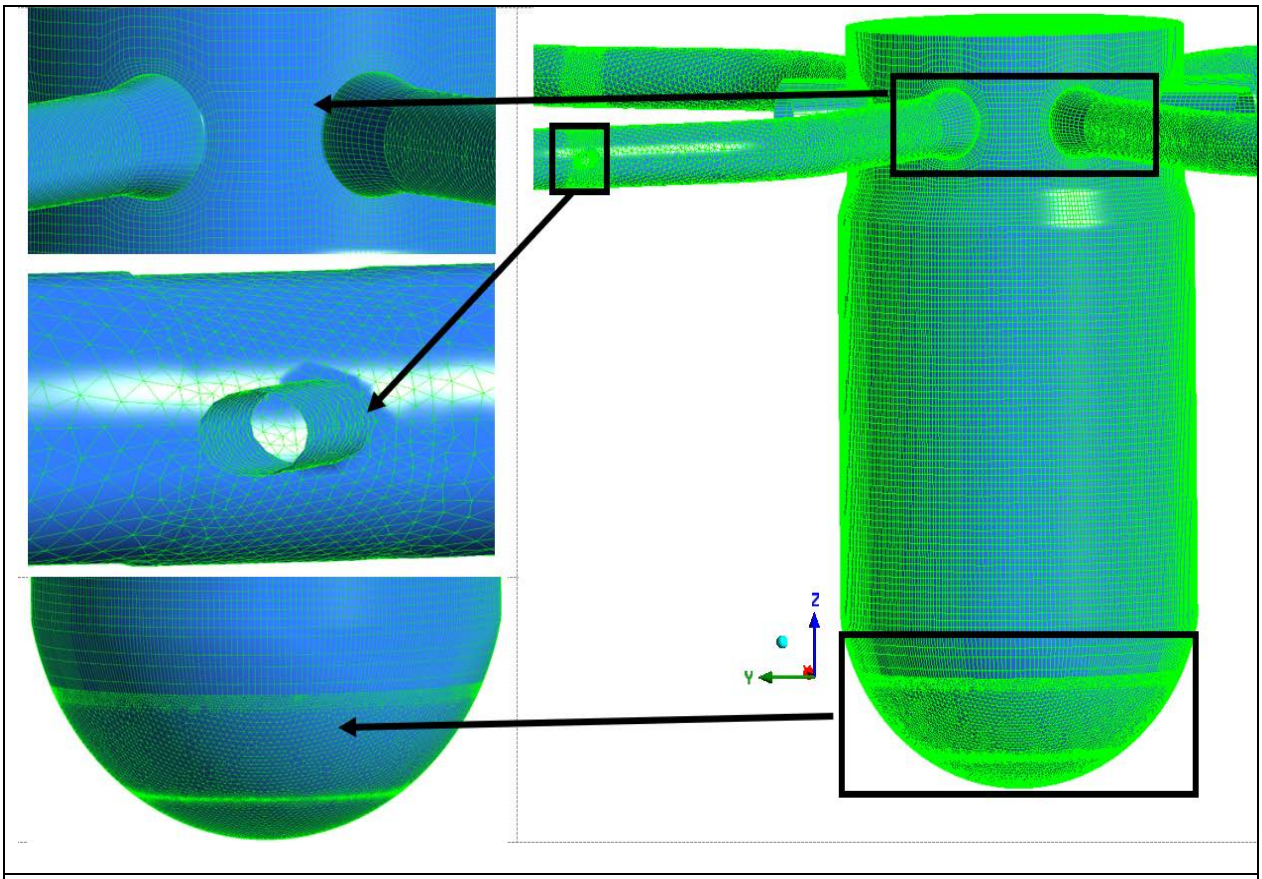

Fig.10.View of mesh

a.

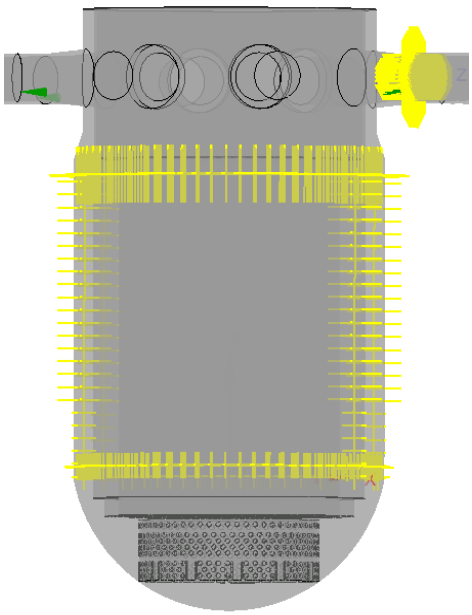

b.

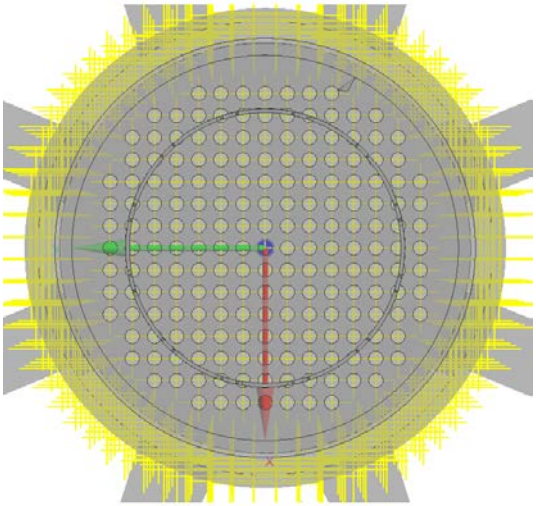

Fig.11. Positions of monitor points, a. In the Downcomer and RPV inlet, b. at Core Inlet

4.4 Boundary conditions

The boundary conditions of the experiment have been accurately reproduced for the simulation **(Table 3)**.

— The velocity of the ECC injection line is 0.64297 m/s. The injection time is from 5 s to 15 s (Dirac impulse) after the start of loop circulation in Cold Leg N°1. The injection is initiated by opening the upstream valve.

— The fluid used in the ECC injection line is glucose-water mixture (10% density difference to tap water density) with a density of 1100 [kg/m3]

— The velocity in Cold Leg N°1 is 0.291 [m/s].

— The other 3 loops are left open.

— Pressure-controlled outlet boundary condition.

— Uniform inlet turbulent intensity profile (5%).

— Upwind discretization scheme for advection terms.

Table 3. d10m10 experiment selected for code validation.

VECC [m3/h]	VECC [m/s]	V loopN°1 [m3/h]	VloopN°1 [m/s]	Density difference Loop / ECC water	Fr (Downcomer)
3.6	0.64	18.5	0.291	1/1.1	0.85

4.5 Numerical solution procedure

In the current study, a convergence criterion of 1×10^{-6} was used to ensure negligibly small iteration errors. The time step used was 0.05 s. The glucose-water mixture, which had a higher density, was used as a tracer. It has been modeled with the multi-component model of Ansys-CFX. In this case, the components share the same velocity, pressure and temperature fields. The properties of the multi-component fluids are calculated assuming that the constituent components form an ideal mixture. The glucose-water mixture is modeled as a component with a different density and viscosity than water. The mass fraction of the glucose-water can be directly related to the mixing scalar described in Eq. (1) (Höhne et al., 2011a). So, the properties of the component are calculated from the mass fractions of the constituent materials and are based on the materials forming an ideal mixture (Ansys-CFX-Solver Modeling Guide, 2020). However, using of simplified models to describe turbulence imposes restrictions on the resolution in space and time that can be used in a CFD calculation. Thus, the mixing scalar has been added to the expression part in CFX-Pre as an

additional variable and calculated by CFX-Solver. The ECC injection has been defined with a Dirac delta function of 10 s duration. The injection is performed at the beginning of the simulation (5 s). Therefore, the fastest transients appear in the first part of the simulations. Consequently, in the following sections, only the initial 50 s will be shown for cold leg and upper downcomer sensors, thus facilitating the comparison of the results.

This leads to modeling errors and numerical errors that give more or less inaccurate results. A higher level of quality assurance in the validation of CFD codes has been achieved by consequently applying BPG (Kliem et al., 2010.; Rohde et al., 2005; NEA, 2015; NEA, 2007).

The overall error of a CFD calculation is a combination of several aspects: grid density, discretization method, time step size, iteration error and the employed mathematical models all have their own effect. The separation of these error components for complex three-dimensional calculation is difficult. For example, discretization errors can act like an additional numerical diffusivity, and can affect the results in a similar way as a too large eddy viscosity arising from an unsuitable turbulence model. Discretization errors can be reduced by using finer grids, higher-order discretization methods and smaller time step sizes. However, in many practical three-dimensional applications, grid- and time step-independent solutions cannot be obtained because of hardware limitations. In these cases, the remaining errors and uncertainties should be quantified as described in the Best Practice Guidelines (BPG) by (Bestion, 2012; NEA, 2015; NEA, 2007). The calculations are performed on workstation with 82 parallel processors CPU 3.66 GHz each, containing 32 GB RAM. The simulated time period is 300s. The used time step, is Δt = 0.05 s.

5. Results and discussions

This paper presents the results of numerical simulations of the ROCOM PTS experiments proposed by the IAEA as an international open reference with the purpose of demonstrate the capability of CFD codes to predict the complex phenomena of mixing flow, a comparison was carried out between the calculated results performed with the commercial code Ansys-CFX. 2022.R1 and the measurements from the experimental setup. In this part the results will be illustrated by quantitative and qualitative simulation assessment versus experiment in different location of sensors.

5.1 Mixing scalar behavior in the cold leg inlet sensor

The measured and calculated mixing scalars are shown in different positions of the sensor located in the RPV inlet in **Fig. 12**. There is a good agreement between the experimental and CFD results for all these selected positions in the grid sensor, despite a small lag between them. In this section, we prove the existence of stratification and an influence of buoyancy on the values of the mixing scalar in the flow during and after injection at the injection branch.

First of all, the positions (top, bottom, right, left) in relation to the sensor shown in Fig.12 (c, d, e, f) are only made to diagnose the influence of buoyancy on the mixing quality in the flow, as seen from these positions that the values at the bottom positions are maximal compared to the values at the top positions, which are minimal. Furthermore, the two points on the right and left have the same value (Fig.12 c, d).

The agreement is also good between the measured and calculated mixing scalar values in the positions located on the left and right sides of the sensor (Fig. 12 (c, d)). For the locations deposited at the top and bottom of the sensor (Fig. 12 (e, f)), the CFD calculation under or overestimate the measured mixing scalars.

For the positions (0602 and 0707) in Fig.12 (a, b), both profiles are identical with the existence of a slight delay for the position (0707) between 20s and 22s. For the position (0602), the CFD simulation underestimates the mixing scalar value compared to the experimental data.

This shows the existence of stratification, where the mixing is very dense in the lower part of the pipe in the cold branch because of a density difference, distinguished by a different increased density compared to the ambient fluid. So we can say that the lower the mixing position, the higher the scalar mixing value.

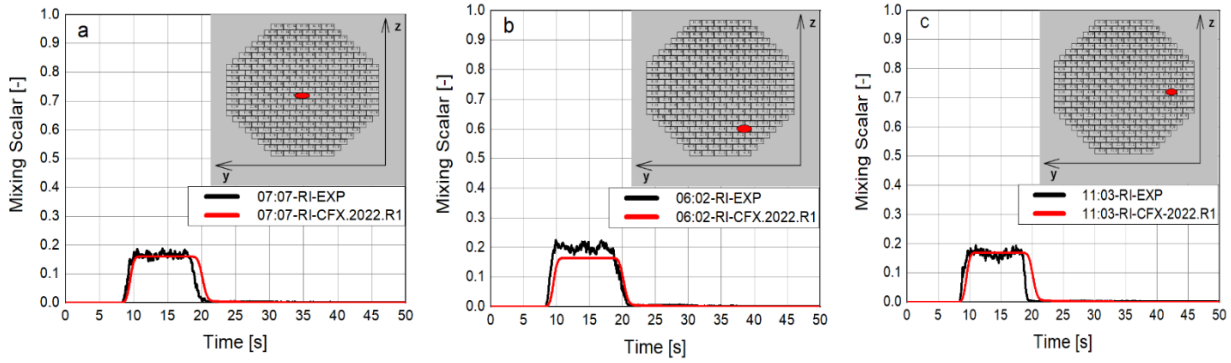

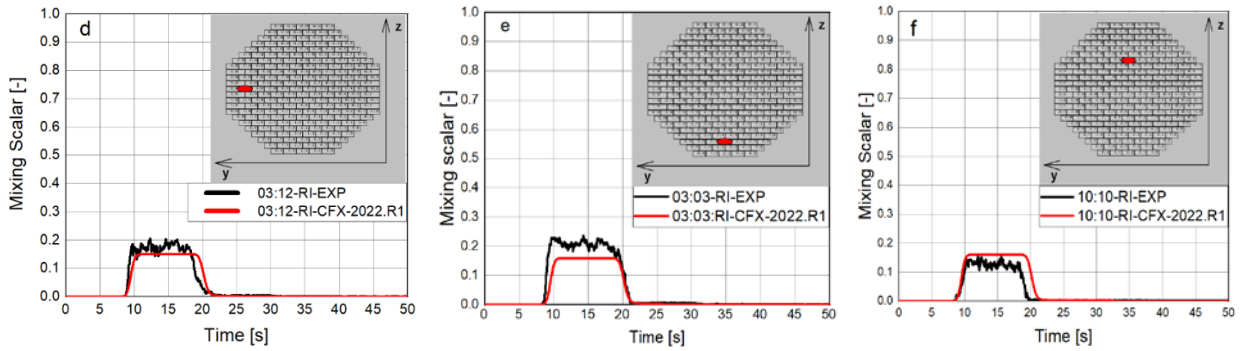

Fig.12. Different local mixing scalar positions in the RPV Inlet sensor.

Globally, the phenomenon of thermal stratified flows occurs when two different layers of the same liquid at different temperatures flow separately in horizontal pipes without appreciable mixing. In our case, this physical system is modulated by injecting a tracer (glucose-water mixture) carrying a high density compared to the fluid circulated in the cold branch.

In **Fig.13**, the ECC first strikes the opposite wall of the injected leg due to the momentum of the jet before being transferred to the cold inlet. After the start of the injection, the shape of the flow in the cold leg changes due to buoyancy effects. Later this is partly mixed with the ambient loop inventory, but mostly propagates toward the reactor inlet at the bottom of the cold leg. During and after the injection period, the ECC water was transported to the reactor inlet using the cold leg. Further of this, the lower density coolant flows in the upper part of the pipe cross-section area and the higher density coolant in its lower part. Accordingly, the thermal stratification in the inlet cold leg was presented qualitatively and accurately by the transient RANS (SST) approach.

in order to inspect the quality of the mixture, the asymmetricity powerfully complicates the flow distribution, which is a consequence of the interaction between the flow from the main pipe and that from the branch pipe. That's why a robust mixing gradient is presented here, despite the pipe elbow Cold Leg N°1 after the branch pipe of ECC injection and before the down-comer entrance enhancing the mixing process. Experimental investigations demonstrate that the gradient at the ROCOM facility is also present in the upper plenum of the RPV due to strong, large-scale vortex structures.

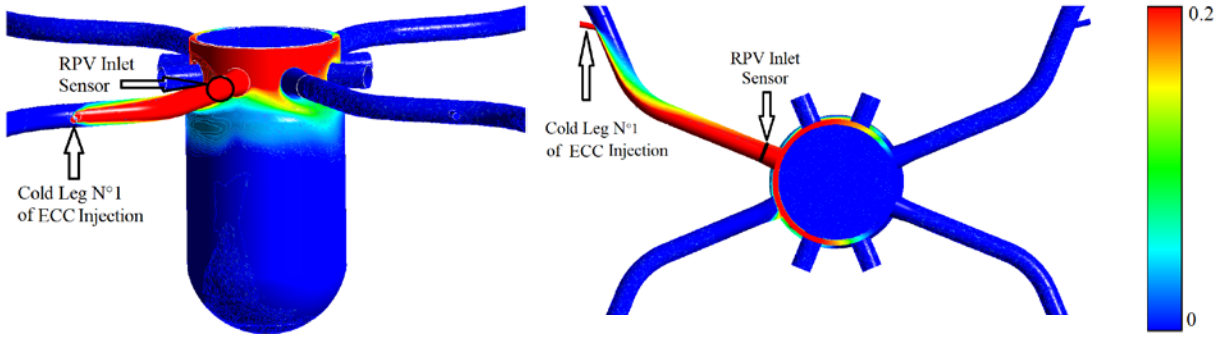

Fig.13. Fig.13. Mixing scalar distribution in the cold leg RPV for t=15s

The stratification at the cold inlet from 5s to 25s is shown in **Fig.14**. It can be observed that the indication of the stratification caused by the density difference between the ECC and the fluid which circulates in loop N°1 strongly depends on buoyancy-driven effects. In addition, the ability of applied CFD code to predict appropriately thermal field is very efficient but still with a perceptible uncertainty. Then the stratification in the cold leg causes the slug to be less diffuse and can causes high temperature gradients and increases thermal stresses of the reactor pressure vessel.

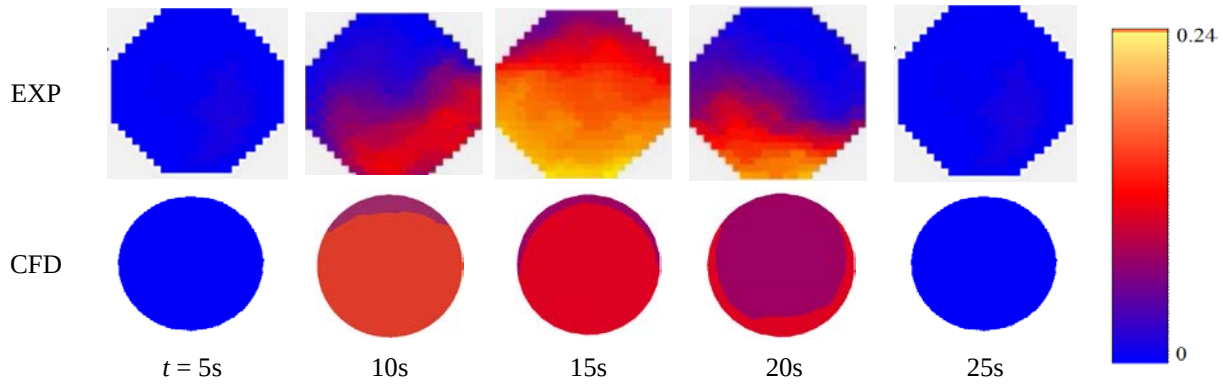

Fig.14. Mixing scalar at different times illustrating stratification flow in the RPV Inlet sensor

5.2 Mixing scalar behavior in the upper downcomer sensor

The second sensor is located at the top of the downcomer and characterized by a ring containing four circular wires **(Fig.4)**. The middle wire placed in the radial middle of the downcomer has been chosen to evaluate the different calculations of the mixing scalar.

Fig.15. represents the variation of the mixing scalar in time in the position of (05:01), which is located under the cold leg N°1 into which the ECC is injected. The reason for focusing on the area under this leg is that the mixing processes at these positions have a significant effect on thermal fatigue. A slight under-prediction of the CFD calculation can be

observed due to the complexity of mixing phenomena in the downcomer. The minor delay happened here indicates quantitatively the uncertainty prediction of CFD in the downcomer according to turbulence mixing complexity. After this unimportant delay, the two curves will have the same behavior until the instant 300s. So, this calculation presented by CFD describes well phenomenon that happened in the upper part of the downcomer.

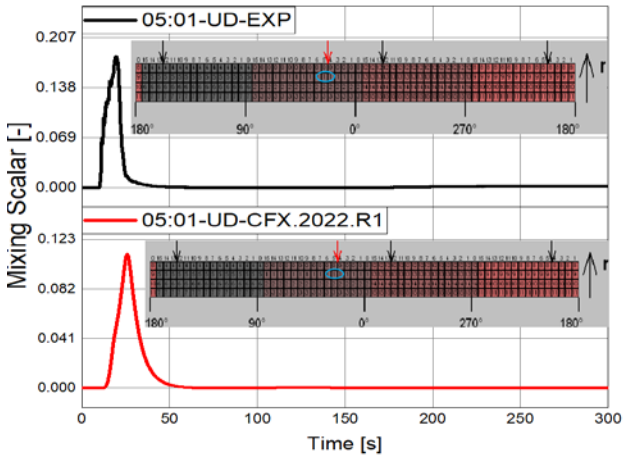

Fig.15. Time history of mixing scalar at the point (05:01) in the middle of upper downcomer

To be consistent with the previous result, three positions below the cold inlet are located radially in the upper downcomer sensor for different azimuthal angles, as shown in **Fig.16**.

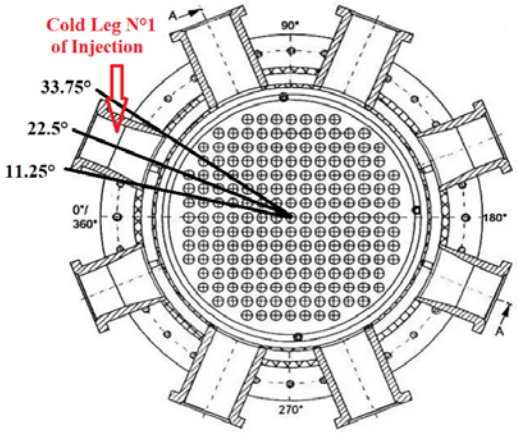

Fig.16. Different azimuthal positions in upper downcomer

We notice globally in all the selected positions that the CFD quantitatively underestimates the experimental results with a modest delay. Moreover, this underestimation is due to the small-scale vortices caused by the turbulence that exists in the downcomer.

For these azimuthal positions in **Fig.17**, the shape of the mixing scalar CFD calculation follows qualitatively the curve of the experiment with a difference in peaks value. For the ECC calculation, the water flows later in the downcomer with minor delay and persist more than the ECC experiment which does not persist as long. The difference between the experimental and CFD at the maximum values is significant. It appears that the use of SST *k-ω* turbulence model led to stable flows. Despite the model's best efforts, its mathematical methods might not be the most appropriate in the given circumstance.

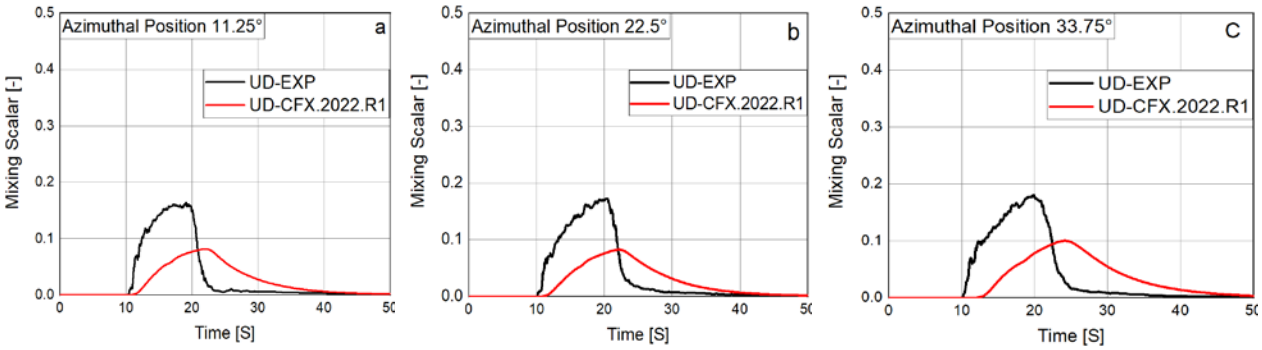

Fig.17. Development of mixing scalar for multi- azimuthal position in the upper downcomer below the Cold Leg N°1 of injection

Fig.18. represents a qualitative comparison of the EXP- CFD mixing scalar distributions in the top sensor in the downcomer. We note that the CFD estimates the distribution of the mixture quite well due to model strength to capture all scales of turbulence phenomenon; in other words, the mixture occupies nearly the same azimuthal surface in the injection side in CFD compared to the experimental results. Moreover, it is observed that the maximum values of the mixture are located near the internal wall of the downcomer, which means that the mixture first hits the inner wall before its descent by the impinging jet phenomenon, which is characterized by a high velocity caused by the slug injection.

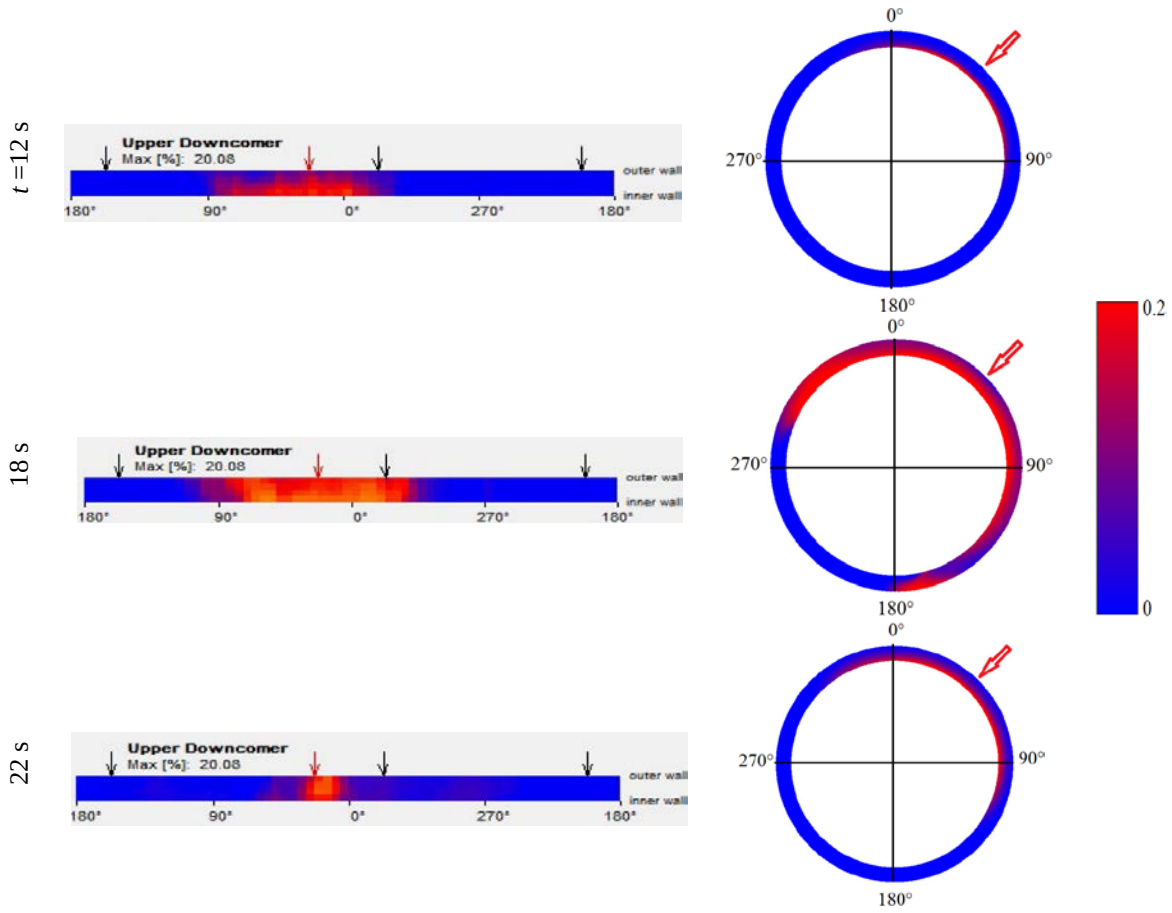

Fig.18. Mixing scalar distribution in the upper downcomer at different times

Fig.19. shows the scalar concentration, indicated by the two sensors in the upper and lower part of the RPV along the circumferential direction from 10s to 45s. The red arrow at the top indicates the position of the cold branch in which the ECC injection was done, while the remaining black arrows correspond to the other cold branches.

The presented experimental and numerical distributions are quite similar. That is, the ECC water in the simulation reaches the upper downcomer at the same time as in the experiment for a given flow rate, and the maximum concentrations in the simulations are in good agreement with the experimental values. The typical patterns of buoyancy-driven flow regime in the downcomer are also predicted correctly. The cooler ECC mixture flows almost

vertically in the upper downcomer, while spreading in the lateral direction in the section below, flowing in a downwards-directed helix around the core barrel. The circumferential spreading is already significant in the upper downcomer position for the impinging jet. This step shows good qualitative agreement between the calculated and experimental ECC coolant mixing models for the gravity-driven plume phenomenon.

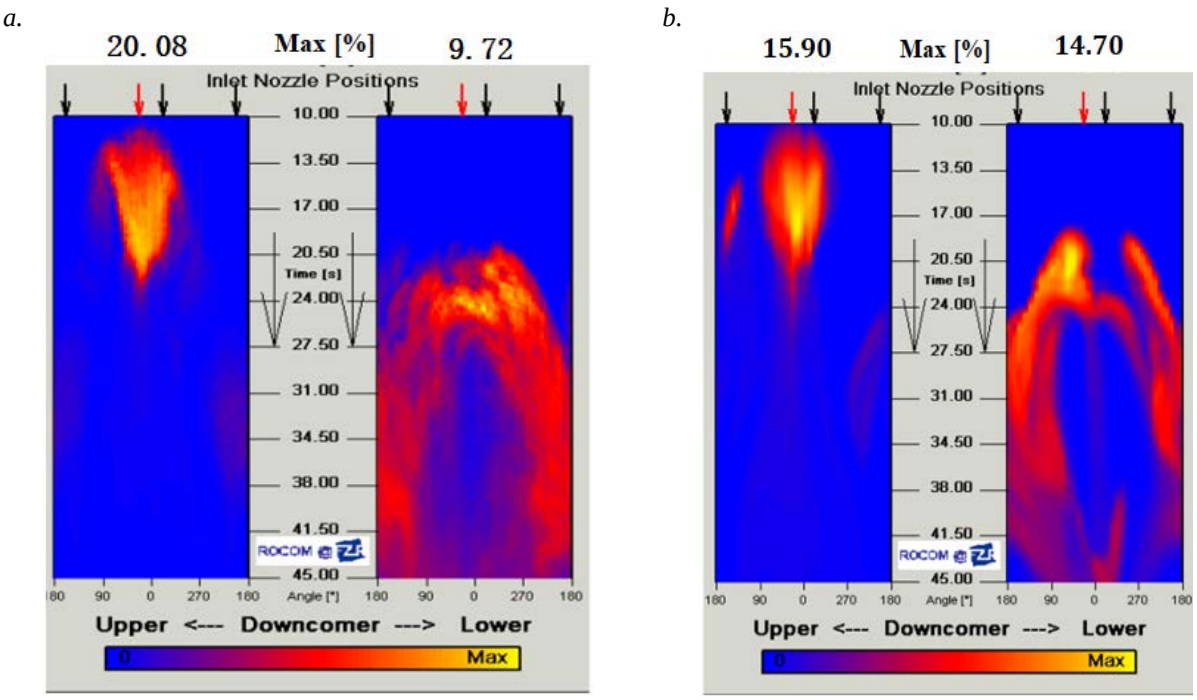

Fig.19. Mixing scalar evolution in the downcomer in ROCOM buoyancy driven mixing tests, a. EXP., b. CFD

The maximum concentration values observed at both downcomer sensors are in the same region, 20.08 % and 9.72 % in the experiment and 15.90 % and 14.70 % in the CFD simulation for the upper and lower downcomer, respectively. Visualizations of the behavior of the ECC water in the downcomer reveals that the ECC water covers a little part of the perimeter of the upper sensor and passes the measuring plane of the lower sensor mainly on the opposite side of the downcomer. As density effects dominate, the area at the top measuring device covered by the ECC water is very small. The ECC water falls straight and passes the sensor in the lower part of the downcomer under the inlet nozzle of the working loop. The phenomenon of stripe detaches from the RPV wall happens when higher cold leg ECC injection rates

are applied, causing deflecting jet. The maximum of the mixing scalar is not located directly below the inlet nozzle; an azimuthal shift of the maximums can be observed because of the asymmetric location of the inlet nozzles.

In **Fig.20**, two vertical planes have been chosen (*xz* and *yz*) in the RPV to study the behavior of the mixing scalar during the test. We see in **Fig. (19, 20)** that the most of the mixing scalar descends through the opposite side of the cold branch. The mixture enters the RPV with a jet force that makes it first hit the inner wall of the RPV, then propagates with a small rotation forming a plume that moves in a counter-clockwise direction.

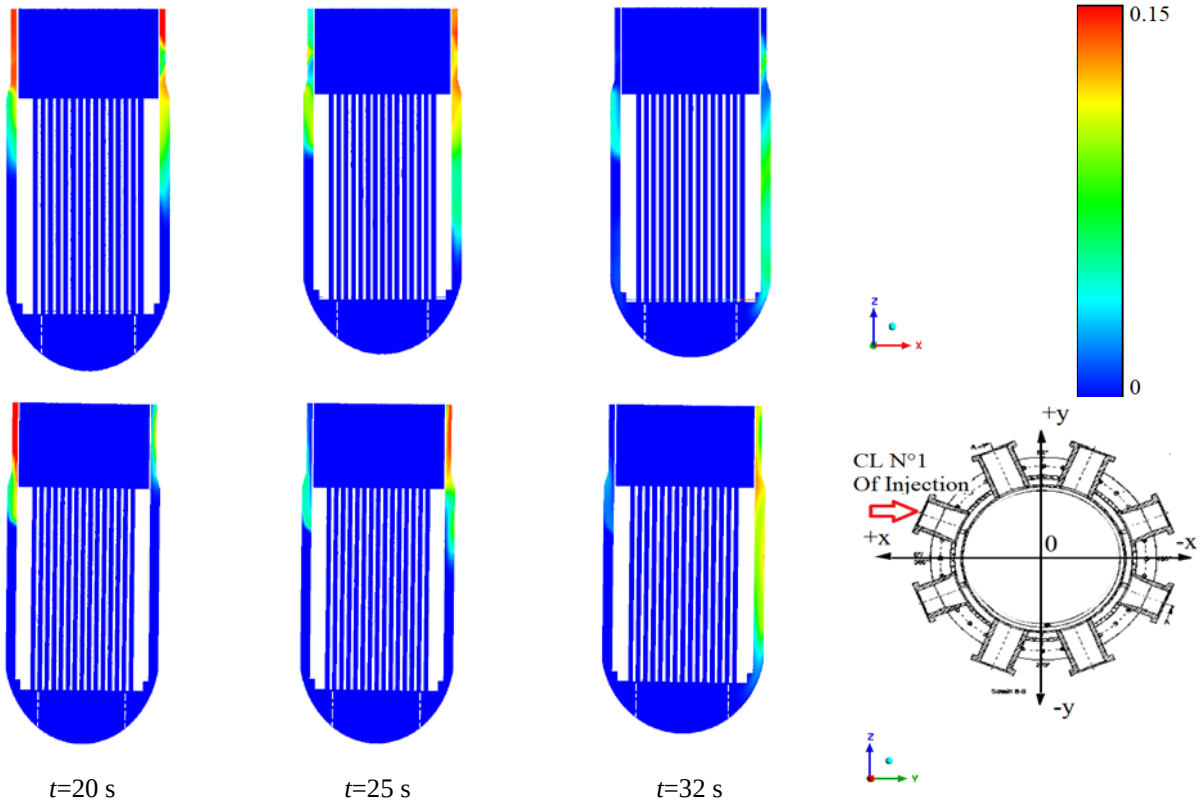

Fig.20. Mixing scalar behavior in the downcomer for the plan *xz* and *yz*

As mentioned, the density difference between the ECC water and primary loop coolant is 10%. In this case, a streak formation of the water with higher density is observed. At the upper sensor, the ECC water covers a much smaller area in the azimuthal sector. The difference in density partially suppresses the propagation of the ECC water in the horizontal direction. When the slug reaches the upper downcomer, unscrews towards the opposite side of the injection, so the most mixing scalar descends on the opposite side of loop N°1. Then the complete mixing falls in an almost straight line and reaches the lower downcomer sensor directly below the nozzle which it entered through. With regard

to the two planes (*xz*) and (*yz*) as seen in **Fig.20**, it is clear that the mixture reaches the lower downcomer and enters the reactor core at the same time for both planes.

5.3 Mixing scalar behavior in the lower downcomer sensor:

The third sensor is located at the bottom of the downcomer and is completely similar to the top sensor. Therefore, 32 circumferential positions have been chosen in the middle of the downcomer to measure the snapshot and azimuthal position of the mixing scalar. As it is known, the calculation CFD is very accurate to estimate the mixing scalar in downcomer when a slight sensitivity existing to small turbulent disturbances at the ECC inlet in the annular space. To verify these data, **Fig.21** illustrates the variation of mixing scalar in time in two points (05:01 and 14:01), by which it is found that the values in the lower downcomer are smaller compared to the upper sensor due to turbulent mixing.

It is clear that the two (**Fig.21** a, b) have a good look qualitatively between CFD and EXP. but compared to the quantitative behavior there is a significant underestimation of CFD related to the physical phenomenon of the turbulence. The physical phenomena that cause the quantitative deficit and disturbance of results have a very strong relationship with the balance of frictional pressure that drops the inertia effects by the direct contact between the inner wall and the mixture in the downcomer.

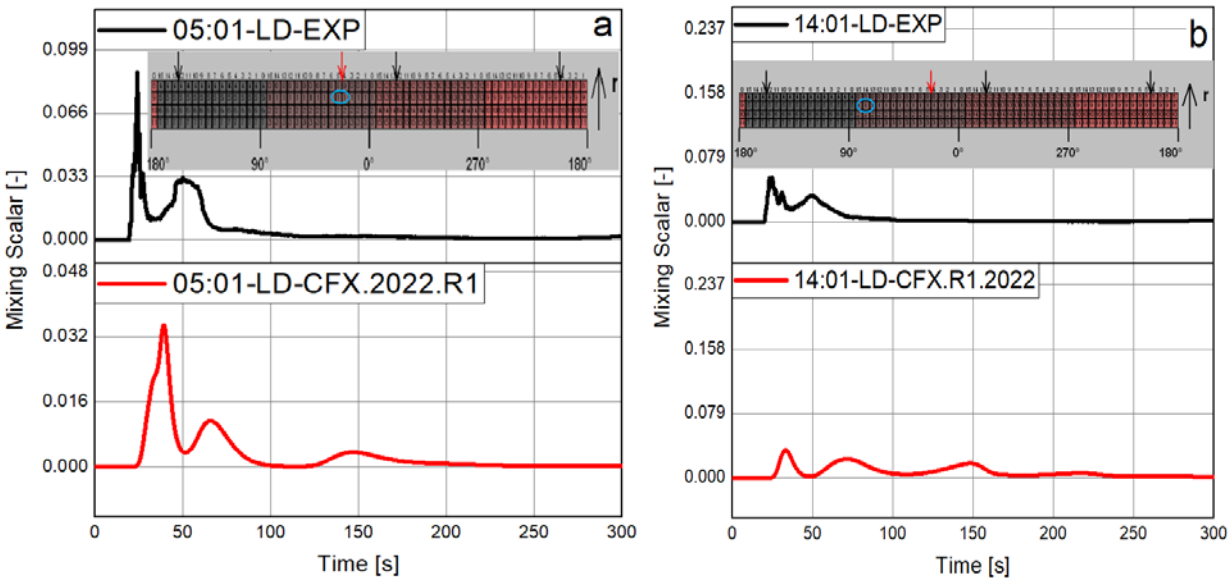

Fig.21. Time history of mixing scalar in the middle of lower downcomer

In order to agree with these results, five azimuthal points have been selected at different positions to monitor the path of the mixing scalar, as shown in **Fig.22**.

in **Fig.22** at positions 11.25° and 22.5° respectively, we note the existence of an underestimation of the part of the CFD in which scalar mixing converges towards infinitesimal values in the curve seen, this convergence is due to the location of these angles which are situated exactly under the cold branch of the ECC injection where there are enormous mixing vortices. In position 33.75°, the CFD estimates quantitatively well the experimental results with a minuscule delay; some of the data with less accuracy illustrate a lack of CFD prediction that signifies that the turbulence is forceful under the injected branch. On the other hand, in positions 45° and 78.75°, the quantitative and qualitative agreement between CFD-EXP is good; therefore, it shows that the turbulence is weaker in these azimuthal positions.

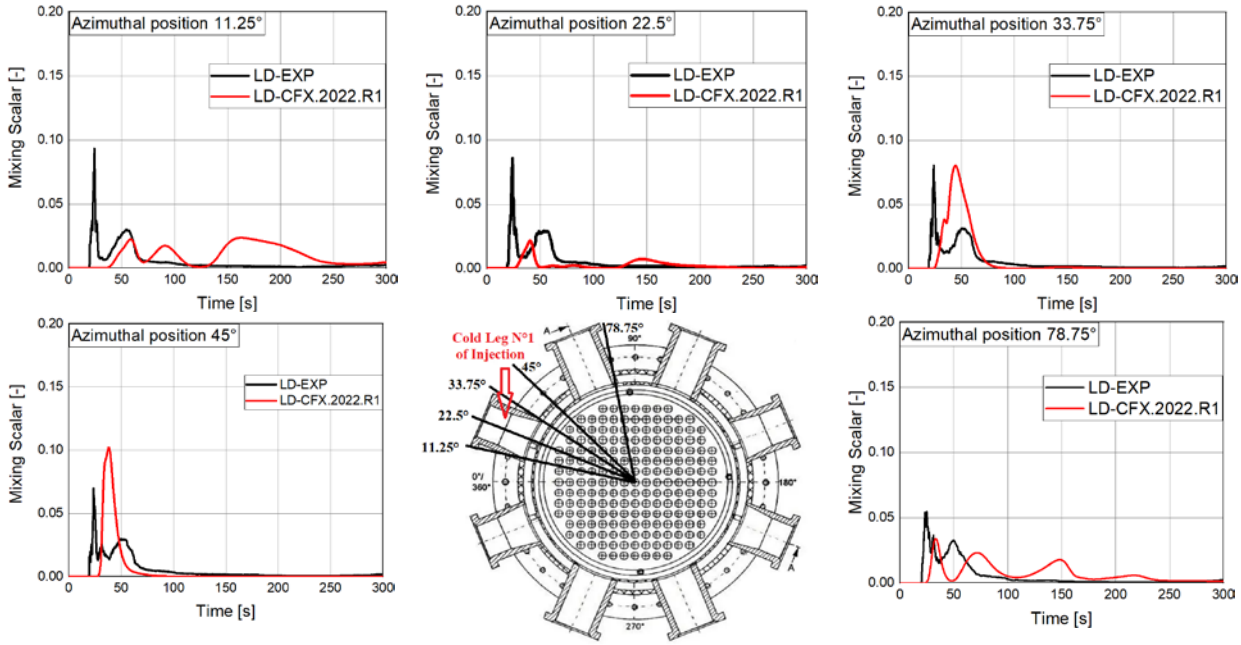

Fig.22. Mixing scalar development in different azimuthal positions in the lower downcomer below the injected cold leg

The shape of the mixing scalar distribution is evidently pseudo-close between the experiments and the numerical results in the comparison in **Fig. 23**, and we then observe that the CFD occupies a quasi-similar area of the mixing scalar distribution engaged by the EXP. This convergence of data is caused by the weakness of the turbulent structure, which is less intense at the lower downcomer position, and probably due to the advantage of the used SST turbulence model in the downcomer. The qualitative and quantitative simulation results from Ansys-CFX. 2022.R1 demonstrate that this CFD code can accurately simulate transport and mixing phenomena, including stratification of fluid flow in reactor coolant, and streaks of coolant with higher difference density in the downcomer.

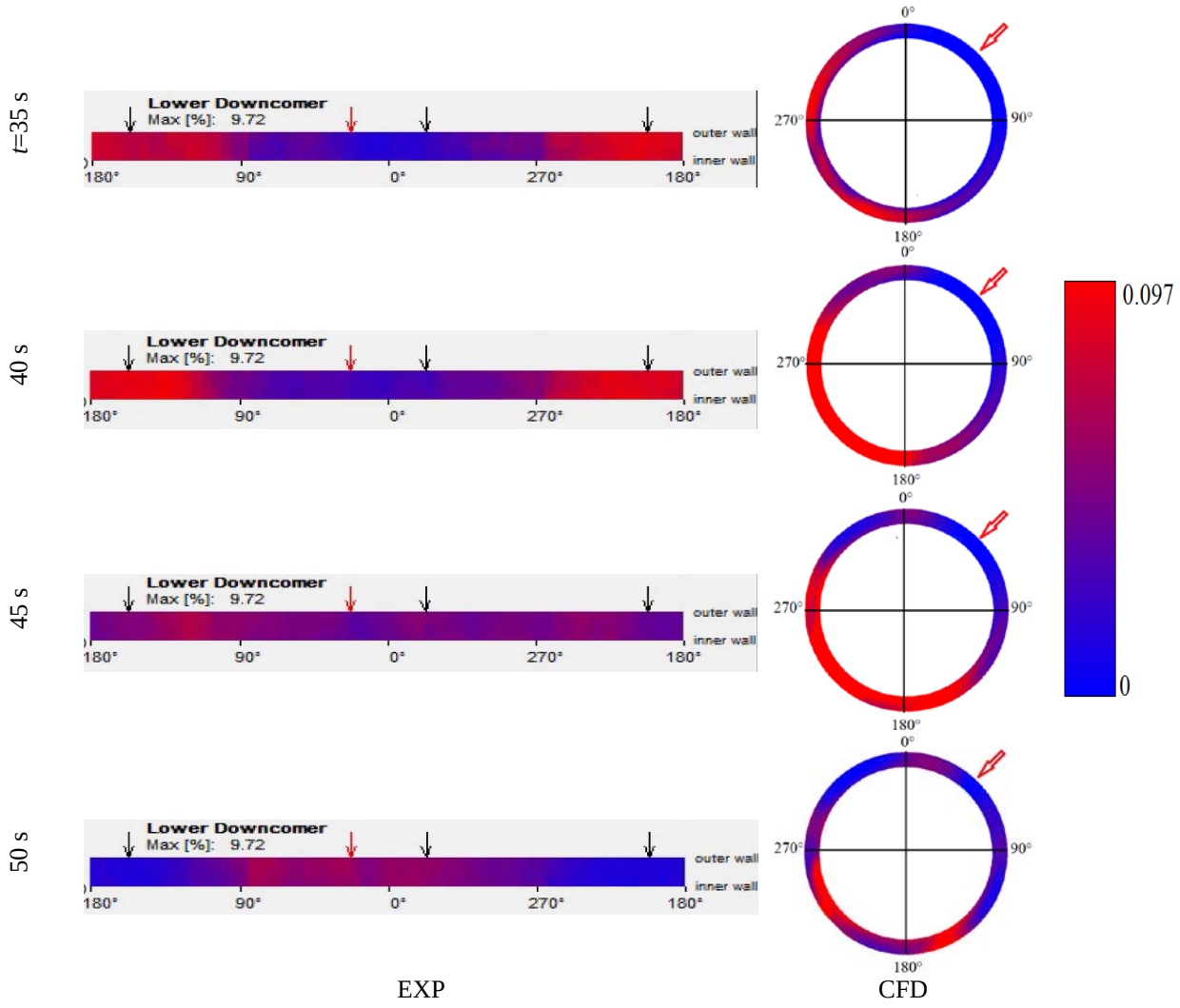

Fig.23. Mixing scalar distribution in the lower downcomer at different times

5.4 Mixing scalar behavior in the Core Inlet sensor:

The last sensor mesh crossed by the mixture is placed at the core inlet of RPV for the aim of measuring the mixing phenomenon that occurred in this section. The transient variation of the mixing slug for a duration of 300s in different positions is shown in **Fig.24**. These graphs generally show a good quality prediction of the mixing distribution due to the effectiveness of the model despite the complexity of the phenomenon and geometry existing in the lower plenum and in the sieve drum.

Firstly, (**Fig.24** a, b, d, e, and h) depict satisfactorily the CFD calculations against experimental results. Consequently, this reasonable agreement reveals that the existence of mixing scalar entering firstly the reactor core with less vortices in this region precisely in the quarter of cold leg of injection. The density differences effect between the tracer slug and

the fluid coolant also shows enhancements of the mixing effects when the slug is heavier and passes through the sieve drum which has a significant effect as a flow resistance in the lower plenum.

Secondly, the calculated maximum mixing scalar values significantly (**Fig.24 (f, g)**) and slightly (**Fig.24 (c)**) exceed the experimental values. Hence, these small differences can be addressed for different reasons, which can intervene in the mixing phenomenon. Belonging to this phenomenon, the existence of a strong swirl on the opposite side of the injected cold leg and under an inactive loop which amplifies the random character of the flow where the mixing was weaker in this region after some time. Furthermore, other effects can happen which cause these inconsequential divergences between CFD calculations and experimental results due to unsteady arbitrary flow. In this calculation, the SST k-ω (RANS) model is used (the *k-ω* model works near the wall and the *k-ε* model works in the bulk flow) investigate mixing effects in the core inlet. This is probably related to the strength of this model residing in its compatibility in the case of low Reynolds.

In almost of these simulations in the core inlet sensor for all positions presented below, the CFD calculation transient predict acceptably the experimental results in this sensor. according to the CFD curve of mixing which was somewhat upper than the experimental values, This was properly a result of the density differences that cause buoyancy under the natural circulation phenomenon between the emergency core coolant (ECC) cold slug and the nuclear power plant primary fluid (NPP).In short, through this model that have been analyzed, it is clear that the model SST predict qualitatively the benchmark results in this subsection.

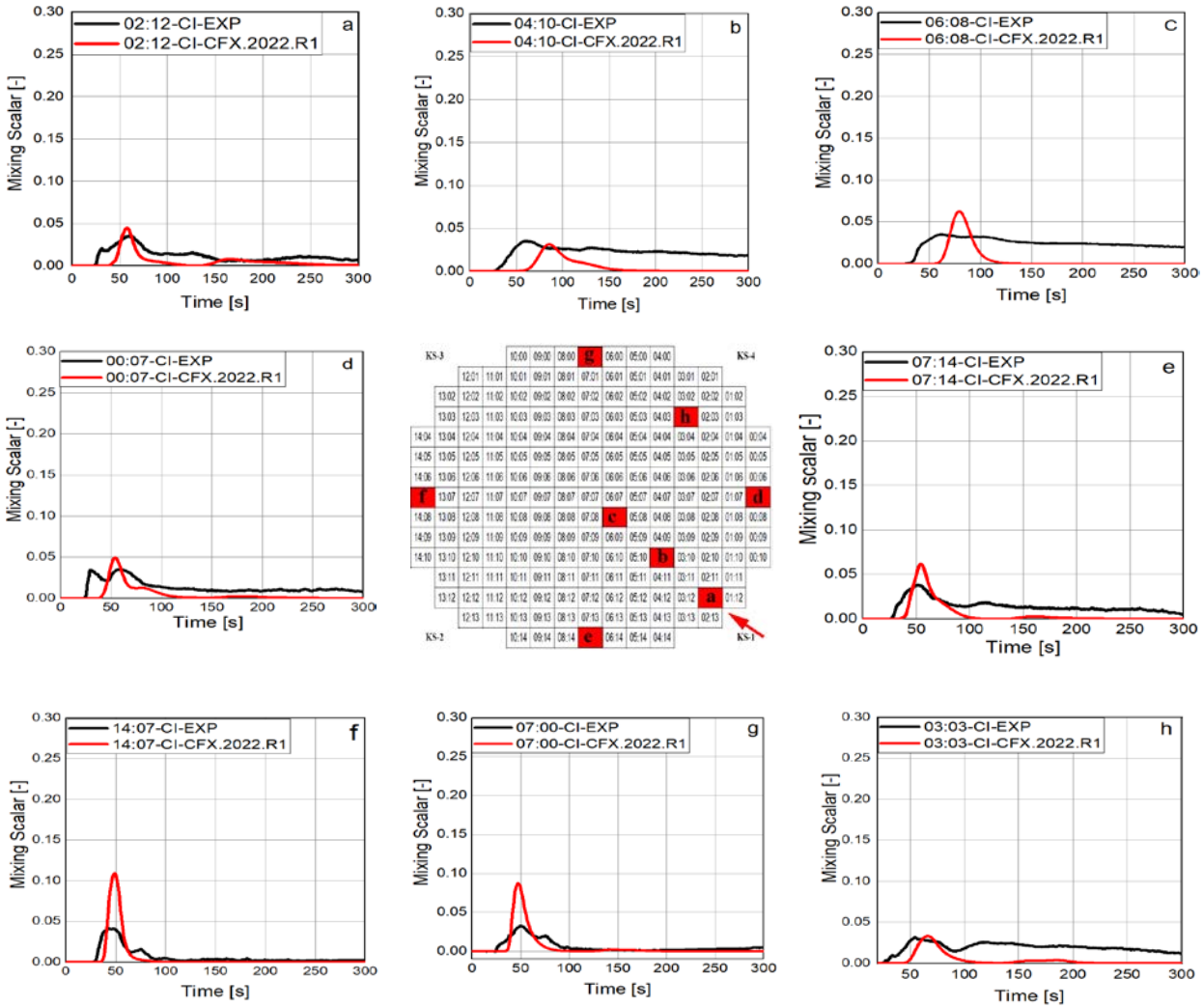

Fig.24. Mixing scalar variation for multi-points in core inlet.

Fig.25 indicates the comparison of qualitative comportment of mixing scalar in the core inlet sensor for some selected instants (38 s, 44 s, 60 s, and 75 s) between CFD calculation and experimental results.

The entrance of mixing in the core has a position very sensitive to the calculation conditions for the ROCOM experiment and CFD computation. The tracer enters firstly the core inlet by two positions on the opposite side of injection loop.

The first small concentration appears at the core inlet in the side located below the inactive loop which is in front of the injection loop, and then, in this side, the mixing enters laterally the core inlet at t= 38s. Hereafter, the mixing progress from the wall of the opposite side of the injection towards the core center inlet until the mixing occupies almost all the core section at t=60s. After this time, the mixture decreases until it is held weakly only at the center of the core until t =

75 s. Furthermore, in this experiment, this process is complemented by a move of the concentration from the opposite side to the side below the active inlet nozzle where there is mainly a rotational movement of the concentration field. This could be relevant in reality, as a core is primarily different radially, regarding enrichment and reactivity.

Consequently, the sector formation and the mixing scalar values are well reproduced qualitatively in the calculation by the effect of the difference indicated in presence of density differences, which allows the mixture to be more uniformly spread over the core inlet. Then, a maximum mixing scalar value at the core inlet of about 4% for experimental and CFD results. That means almost of mixing fluid has been well mixed.

The morphology of the tracer concentration distribution at the core inlet was correctly described for the statements t= 38 s and 44 s, but for the instants t= 60 s and 75 s significant differences can be observed. It is evident how the geomorphology of the perturbation affecting the core inlet is related to the flow distribution in the downcomer behavior. The flow distribution in the core inlet and its accurate numerical prediction is an important task due to the well-known limitations of the turbulence modelling based on the Reynolds-Averaged Navier-Stokes approach. There is a challenging with the accuracy of WMS which is much larger than Kolmogorov microscale length that are the smallest scales in the turbulent flow of fluids. Mixing having vortex length scales smaller than WMS resolution cannot be demonstrated and can be defined as incomplete mixing. It is assumed that the majority of turbulent mixing occurs in the flow existing with scales length greater than WMS resolution.

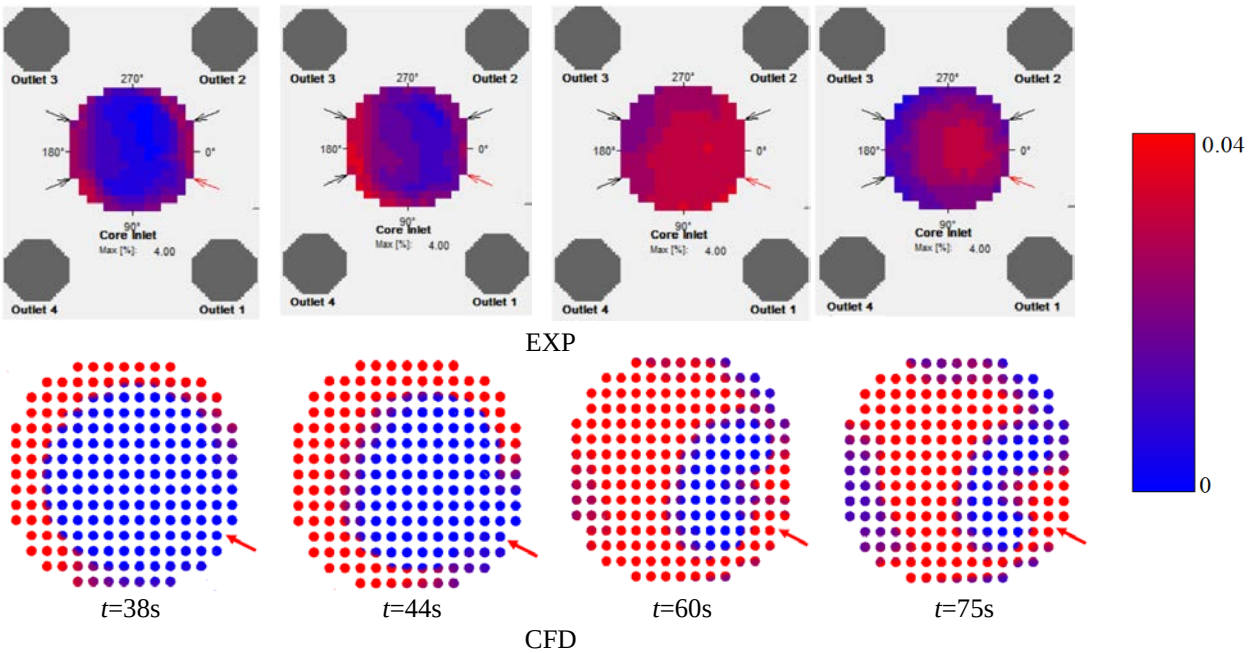

Fig.25. Mixing distribution in the core inlet for different times between Experimental and CFD

In this next part, two perpendicular and intersecting planes (xz and yz) have been chosen with the objective of confirming the previous qualitative observation that was done at the core inlet and to demonstrating the behavior of mixing in the whole reactor core. For this goal and in the same context, (**Fig.26**) and (**Fig.27**) illustrate mixing scalar snapshots in these two planes mentioned above.

Initially, the qualitative behavior of mixing manifests in a very efficient way such that, in the (xz) plane, a good mixing quality is observed because there is not a strong scalar mixing gradient in the reactor core. Besides, this last observation is very required for the safety of the core when the temperature will be treated as a variable.

The mixing scalar enters the core at t= 50 s and leaves it at t= 120 s on this plane (**Fig.26**). According to the data of this (xz) plane, the mixture during its trajectory almost occupies the whole core. This occupation is caused by the position of the cold inlet branch, which is very close to this plane with an inclination of 22.5° between them, and due to the injection force accompanied by jet impingement when the ECC slug is injected in the cold leg. The coolant mixing has been improved by the sieve drum, which contains smaller holes and induces extra resistance for the coolant flow, which will deteriorate the natural circulation ability of the reactor. Also, the passage of the mixture in the lower plenum decreases the gradient and improves the mixing.

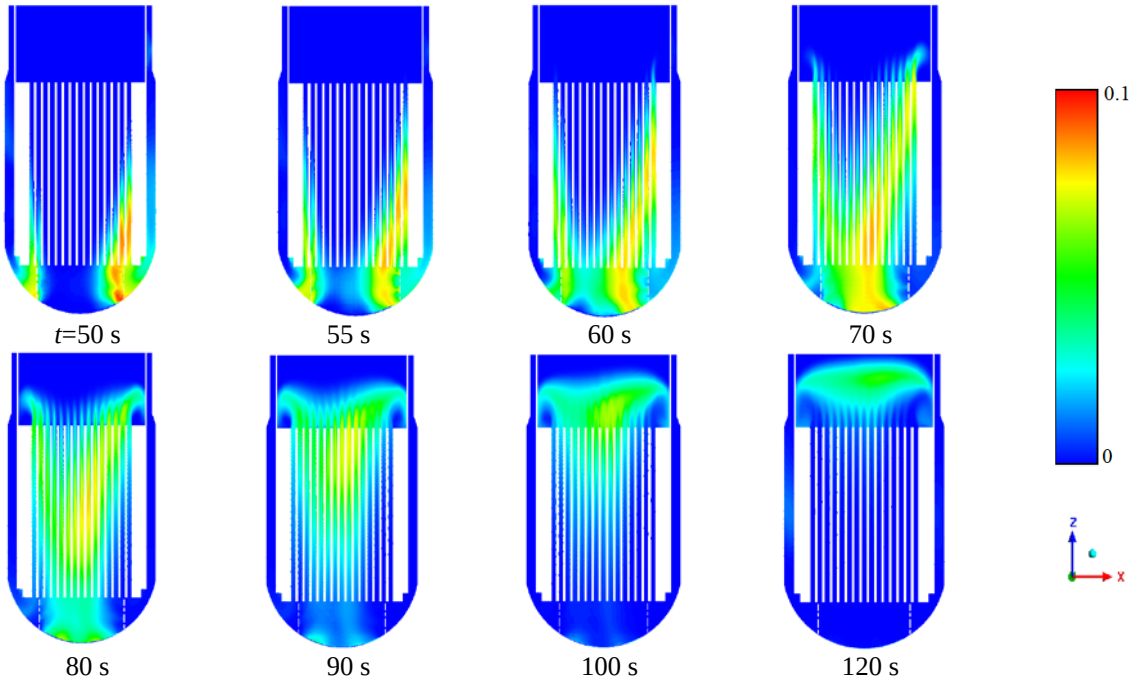

Fig.26. Instantaneous mixing scalar distribution in the core reactor on the (xz) plane

The mixing scalar distribution is shown on the (yz) plane in **Fig.27**. The mixture residues in the core for 135 s, from t= 45 s to t= 180 s, with a significant mixing scalar gradient between t= 45 s and 70 s. After this period, between t= 90s and 180 s, the mixing scalar does not reach such high values as in the early phase of the transient. This means the slug is well mixed with the ambient fluid. Knowing that the mixing in this passage occupies almost the reactor core, in the same hand, The maximum gradient of the mixing scalar is located much more directly to the core side of the reactor, this behavior is related to the one done in the downcomer, where the mixing aligns forming a plume in the side opposite to the injection branch.

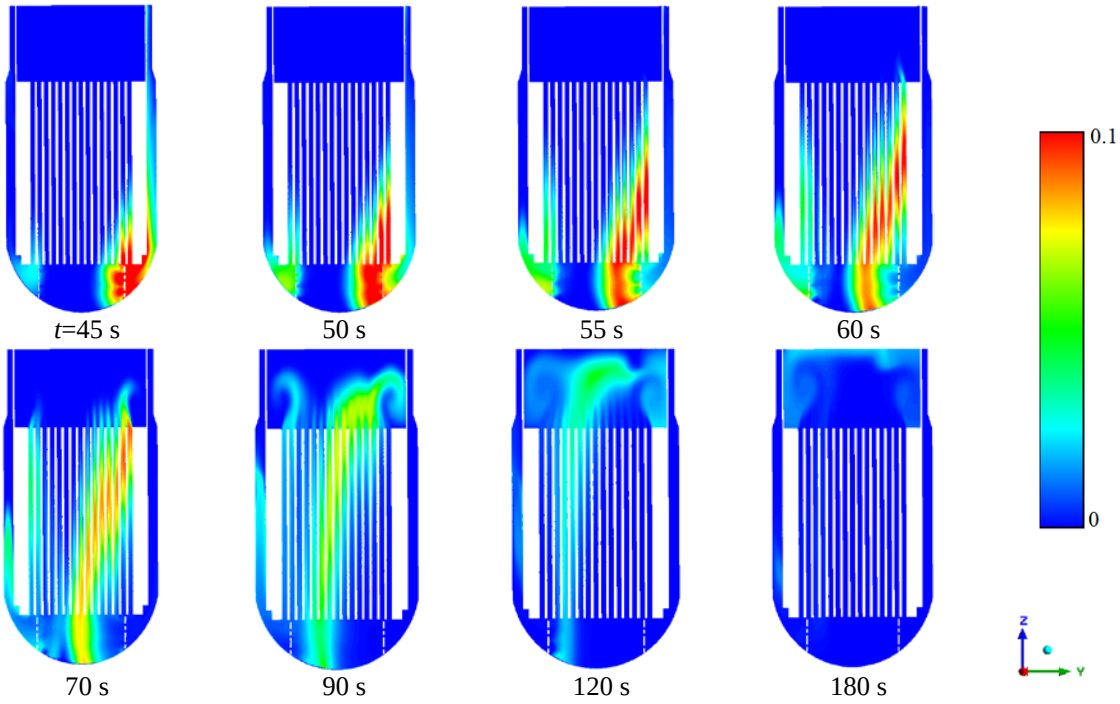

Fig.27. Instantaneous mixing scalar distribution in the core reactor on the (yz) plane

Conclusion

The experimental data (d10m10) were compared with the numerical results of the Ansys-CFX. 2022.R1 CFD software package. This test PTS presents buoyancy driven that produce the buoyancy source terms which are included in the transport equations for the turbulent kinetic energy. Therefore buoyancy affected was investigated under simulated natural circulation conditions at the test facility ROCOM.

The results of the experiments and the numerical calculations show that mixing strongly depends on buoyancy effects. In the evaluation between experiments and CFD calculations, the mixing scalar comportment in the perturbed regions, in the cold leg inlet, in downcomer and in the core inlet, was well predicted qualitatively, and was passably predicted

quantitatively. These outcomes confirm our determination in which the model has been correctly implemented in the CFX code to better predict the complex mixing phenomena that can lead to accidental scenarios affecting the integrity of nuclear facilities. The main findings are summarized as follows:

- The Ansys-CFX. 2022.R1 calculations show a good qualitative agreement with the experimental results, knowing that the better results were obtained, firstly for the cold leg, then for the downcomer, then for the core inlet.
- The model used illustrates reasonably the EXP-CFD pattern in the cold branch sensor of RPV. Additionally, it makes a satisfactory case for the very obvious stratification phenomenon by the mixing scalar variation values for different positions in the top, bottom, right and left in this sensor. Therefore, it is deduced that the mixing scalar values will be higher in the low positions of the sensor at the cold inlet, and will be lower in the high positions because of the density difference and stratification effect.
- The model predictions are following better the profile of the experimental data in the downcomer and core inlet, which has been used to predict transient mixing and capture the complex vortex structures in turbulent flows for conditions where natural circulation is a dominant factor. Acceptable qualitative outcomes are shown by this model in the downcomer and core inlet for the whole trajectory the mixing took, which reveals good capability to predict thermal fields in PWRs.
- Density effects illustrate an important role during natural circulation with ECC injection, producing a stratification during the slug injection in PWRs, The SST k- ω turbulence model looks to analyze the more challenging cases in the mixed convection regime in annular space, where buoyancy forces will be calculated additionally and precisely. This demonstrates the way that the mixing of coolant streams is impacted by density differences. For this reason, it is considered to be a crucial parameter in identifying susceptible PTS areas.

Acknowledgments

The authors are grateful to the CRNB for supply this work by enabling to use the cluster (Ansys-CFX. 2022.R1 with License) during the simulation period. They also acknowledge the ROCOM test facility team at Helmholtz-Zentrum Dresden-Rossendorf (HZDR) institute for providing the experimental benchmark data for PTS (d10m10) event, and a CAD file of the test ROCOM geometry.

Nomenclature

Abbreviation

BPG	Best Practise Guidelines
CAD	Computer Aided Design
CFD	Computational Fluid Dynamics
CFX	Commercial Computational Fluid Dynamics Code
CPU	Central Processing Unit
ECC	Emergency Core Cooling (System)
LOCA	Loss of Coolant Accident
SB-LOCA	Small Break- Loss of Coolant Accident

EXP	Experiment
RI	Reactor Inlet
UD	upper downcomer
LD	lower downcomer
CI	Core Inlet
SST	Shear Stress Transport
URANS	Unsteady state Reynolds-Averaged Navier-Stokes
CRP	Coordinate Research Project
CRNB	Nuclear Research Center of Birine
HZDR	Helmholtz-Zentrum Dresden-Rossendorf
IAEA	International Atomic Energy Agency
NEA	Nuclear Energy Agency
NPP	Nuclear Power Plant
PTS	Pressurized Thermal Shock
ROCOM	Rossendorf Coolant Mixing Test Facility
RPV	Reactor Pressure Vessel
WMS	Wire Mesh Sensor
Fr	Froude number
MSLBA	Main Steam Line Break Accident
CATHARE	Advanced Thermo-Hydraulic Code for Water Reactor Accidents
TRACE	Turbomachinery Research Aerodynamic Computational Environment
ATHLET	Analysis of Thermal-hydraulics of Leaks and Transients

Indices

0	unaffected coolant
1	the disturbed loop
t	time
x	x coordinate
y	y coordinate
z	z coordinate

References

Ansys-CFX -Solver Modeling Guide, 2020.

IAEA-TECDOC-1908, 2020. Benchmarking of Computational Fluid Dynamics Codes for Reactor Vessel Design. (VIENNA,). https://www-pub.iaea.org/MTCD/Publications/PDF/TE-1908_web.pdf

J. Mahaffy, B. Chung, C. Song, F. Dubois, E. Graffard, F. Ducros, M. Heitsch, M. Scheuerer, M. Henriksson, E. Komen, F. Moretti, T. Morii, P. Muehlbauer, U. Rohde, B. L. Smith, T. Watanabe, G. Zigh, 2015. Organization for Economic Co-operation and Development, Best Practice Guidelines for the use of CFD in Nuclear Reactor Safety Applications. NEA. JT03370465.

Bestion, D., 2012. Applicability of two-phase CFD to nuclear reactor thermalhydraulics and elaboration of Best Practice Guidelines. Nuclear Engineering and Design 253, 311–321. https://doi.org/10.1016/j.nucengdes.2011.08.068.

Bieder, U., Feng, Q., Höhne, T., 2016. Analysis of buoyancy-driven flow in the ROCOM test facility. Energy Procedia 127, 44–53. doi.org/10.1016/j.egypro.2017.08.062.

Bousbia Salah, A., Ceuca, S.C., Puragliesi, R., Mukin, R., Grahn, A., Kliem, S., Vlassenbroeck, J., Austregesilo, H., 2018. Unsteady Single-Phase Natural-Circulation Flow Mixing Prediction Using 3-D Thermal-Hydraulic System and CFD Codes. Nucl Technol 203, 293–314. https://doi.org/10.1080/00295450.2018.1461517.

Čarija, Z., Ledić, F., Sikirica, A., Niceno, B., 2020. CFD study of the PTS experiment in ROCOM test facility. Nuclear Engineering and Technology 52, 2803–2811. https://doi.org/10.1016/j.net.2020.06.002.

Chouhan, R., Kumar Kansal, A., Kumar Maheshwari, N., Sharma, A., 2021. Computational studies on pressurized thermal shock in reactor pressure vessel. Ann Nucl Energy 152. https://doi.org/10.1016/j.anucene.2020.107987.

Farkas, I., Hutli, E., Farkas, T., Takács, A., Guba, A., Tóth, I., 2016. Validation of Computational Fluid Dynamics Calculation Using Rossendorf Coolant Mixing Model Flow Measurements in Primary Loop of Coolant in a Pressurized Water Reactor Model. Nuclear Engineering and Technology 48, 941–951. https://doi.org/10.1016/j.net.2016.02.017.

Grunwald, G., Höhne, T., Prasser, H.-M., Richter, K., Weiss, F.-P., 1999. investigation of coolant mixing in pressurized water reactor at the Rossendorf mixing test facility ROCOM. INIS Volume 31, 1-6.

Höhne, T., Kliem, S., 2022. Numerical Analysis Related to the ROCOM Pressurized Thermal Shock Benchmark. Fluids 8, 4. https://doi.org/10.3390/fluids8010004.

Höhne, T., Kliem, S., Bieder, U., 2018. IAEA CRP benchmark of ROCOM PTS test case for the use of CFD in reactor design using the CFD-Codes Ansys-CFX and Trio-CFD. Nuclear Engineering and Design 333, 161–180. https://doi.org/10.1016/j.nucengdes.2018.04.017.

Höhne, T., Kliem, S., Bieder, U., 2006. Modeling of a buoyancy-driven flow experiment at the ROCOM test facility using the CFD codes CFX-5 and Trio_U. Nuclear Engineering and Design 236, 1309–1325. https://doi.org/10.1016/j.nucengdes.2005.12.005.

Höhne, T., Kliem, S., Bieder, U., Prasser, H.M., 2004. Validation of Trio_U - Numerical simulations of a rocom buoyancy driven test case. Paper presented at 12th International Conference on Nuclear Engineering Washington D.C. USA, 25-29 April 2004. 46881, 811–822. https://doi.org/10.1115/icone12-49487.

Höhne, T., Kliem, S., Rohde, U., 2011. Buoyancy-driven mixing studies of natural circulation flows using rossendorf coolant mixing model experiments and CFD. Chem Ing Tech 83, 1282–1289. https://doi.org/10.1002/cite.201100035

Höhne, T., Kliem, S., Vaibar, R., 2008. experimental and numerical modeling of transition matrix from momentum to buyancy-driven flow in a pressurized water reactor. Paper presented at Proceedings of the 16th International Conference on Nuclear Engineering, Orlando, Florida, USA, 11-15 May 2008;

IAEA, 2022. Nuclear Energy Series, Summary Review on the Application of Computational Fluid Dynamics in Nuclear Power Plant Design, No. NR-T-1.20. STI/PUB1932.

Kliem, S., Höhne, T., Rohde, U., Weiss, F.-P., 2010. expriments on slug mixing under natural circulation conditions at the ROCOM test facility using high resolution measurement technique and numerical modeling. Nuclear Engineering and Design 240, 2271–2280. https://doi.org/10.1016/j.nucengdes.2009.11.015.

Kliem, S., Sühnel, T., Rohde, U., Höhne, T., Prasser, H.M., Weiss, F.P., 2008. Experiments at the mixing test facility ROCOM for benchmarking of CFD codes. Nuclear Engineering and Design 238, 566–576. https://doi.org/10.1016/j.nucengdes.2007.02.053.

Loginov, M.S., Komen, E.M.J., Höhne, T., 2011. Application of large-eddy simulation to pressurized thermal shock: Assessment of the accuracy. Nuclear Engineering and Design 241, 3097–3110. https://doi.org/10.1016/j.nucengdes.2011.05.027.

Loginov, M.S., Komen, E.M.J., Kuczaj, A.K., 2010. Application of large-eddy simulation to pressurized thermal shock problem: A grid resolution study. Nuclear Engineering and Design 240, 2034–2045. https://doi.org/10.1016/j.nucengdes.2010.03.023.

Menter, F.R., 1994. Two-equation eddy-viscosity turbulence models for engineering applications. AIAA Journal 32, 1598–1605. https://doi.org/10.2514/3.12149.

Pandazis, P., Ceuca, S.C., Schoeffel, P.J., Hristov, H. V, 2015. Investigation of Multidimensional flow mixing phenomena in the reactor pressure vessel with the system code ATHLET. Paper presented at 16th International Topical Meeting on Nuclear Reactor Thermal Hydraulics, Chicago, IL, USA, 30 August-04 September 2015, Nureth-16, 3378-3391(2015).

Prasser, H.-M., Böttger, A., Zschau, J., 1998. A new electrode-mesh tomograph for gas-liquid flows, Flow Measurement and Instrumentation 9, 111–119. https://doi.org/10.1016/S0955-5986(98)00015-6

Prasser, H.M., Grunwald, G., Höhne, T., Kliem, S., Rohde, U., Weiss, F.P., 2003. Coolant mixing in a pressurized water reactor: Deboration transients, steam-line breaks, and emergency core cooling injection. Nucl Technol 143, 37–56. https://doi.org/10.13182/NT03-A3396

Prasser, H.-M., Krepper, E., Lucas, D., 2002. Evolution of the two-phase flow in a vertical tube-decomposition of gas fraction profiles according to bubble size classes using wire-mesh sensors, Int. J. Therm. Sci 41(1), 17–28. https://doi.org/10.1016/S1290-0729(01)01300-X

Prasser, H.-M., Scholz, D., Zippe, C., 2001. Bubble size measurement using wire-mesh sensors, Flow Measurement and Instrumentation 12 (4), 299–312. https://doi.org/10.1016/S0955-5986(00)00046-7.

Puragliesi, R., 2020. Assessment of a URANS CFD model for gravity driven flows: A comparison with OECD/PKL2 ROCOM experiments. Nuclear Engineering and Design 356, 110365. https://doi.org/10.1016/j.nucengdes.2019.110365.

Rohde, U., Höhne, T., Kliem, S., Hemström, B., Lillington, J., Scheuerer, M., Toppila, T., Dury, T., Remis, J., Muhlbauer, P., Toth, I., Elter, J., Bezrukov, Y., 2005. Fluid mixing and flow distribution in the reactor circuit (FLOMIX-R). Institute of Safety, 27.

Rohde, U., Kliem, S., Höhne, T., Karlsson, R., Hemström, B., Lillington, J., Toppila, T., Elter, J., Bezrukov, Y., 2005. Fluid mixing and flow distribution in the reactor circuit, measurement data base. Nuclear Engineering and Design 235, 421–443. https://doi.org/10.1016/j.nucengdes.2004.08.045.

Rohde, Ulrich, H.-Z., Weiss, F.-P., Prasser, H.-M., Grunwald, G., Höhne, T., Kliem, S., Rohde, U, Weiss, F.-P., F., 2002. Coolant mixing in a PWR-de-boration transients, steam line breaks and emergency core cooling injection-experiments and analyses. https://www.researchgate.net/publication/236445436.

Scheuerer, M., Heitsch, M., Menter, F., Egorov, Y., Toth, I., Bestion, D., Pigny, S., Paillere, H., Martin, A., Boucker, M., Krepper, E., Willemsen, S., Muhlbauer, P., Andreani, M., Smith, B., Karlsson, R., Henriksson, M., Hemstrom, B., Karppinen, I., Kimber, G., 2005. Evaluation of computational fluid dynamic methods for reactor safety analysis (ECORA). Nuclear Engineering and Design 235, 359–368. https://doi.org/10.1016/j.nucengdes.2004.08.049

J. Mahaffy, B. Chung, C. SongF. Dubois, E. Graffard, F. Ducros, M. Heitsch, M. Scheuerer, M. Henriksson, E. Komen, F. Moretti, T. Morii, P. Muehlbauer, U. Rohde, B. L. Smith, T. Watanabe, G. Zigh, 2007. Organisation for Economic Co-operation and Development, Best Practice Guidelines for the use of CFD in Nuclear Reactor Safety Applications. NEA. JT03227125, 15-May-2007.

Wang, M., Wang, Y., Tian, W., Qiu, S., Su, G.H., 2021. Recent progress of CFD applications in PWR thermal hydraulics study and future directions. Ann Nucl Energy 150, 107836. https://doi.org/10.1016/j.anucene.2020.107836

Wei, Z., Ničeno, B., Puragliesi, R., Fogliatto, E., 2022. Assessment of turbulent heat flux models for URANS simulations of turbulent buoyant flows in ROCOM tests. Nuclear Engineering and Technology 54, 4359–4372. https://doi.org/10.1016/j.net.2022.07.009